Conceptual Design of a Thrust-Vectoring Tailcone for Underwater Robotics

by

Michael T. Nawrot

Submitted to the
Department of Mechanical Engineering
in Partial Fulfillment of the Requirements for the Degree of

Bachelor of Science in Mechanical Engineering

at the

Massachusetts Institute of Technology

June 2012

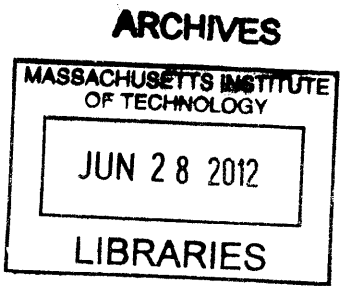

Signature of Author.....
Department of Mechanical Engineering
June 1, 2012

Certified by.....
Amos G. Winter
Postdoctoral Research Associate, MIT-SUTD International Design Center
Thesis Supervisor

Accepted by.....
John H. Lienhard V
Samuel C. Collins Professor of Mechanical Engineering
Undergraduate Officer

Conceptual Design of a Thrust-Vectoring Tailcone for Underwater Robotics

by

Michael T. Nawrot

Submitted to the Department of Mechanical Engineering on June 1, 2012
in Partial Fulfillment of the Requirements for the Degree of

Bachelor of Science in Mechanical Engineering

ABSTRACT

Thrust-vectoring on Autonomous Underwater Vehicles is an appealing directional-control solution because it improves turning radius capabilities. Unfortunately, thrust-vectoring requires the entire propulsion system be articulated in two degrees of freedom. Consequently, substantial internal volume must be utilized for this system, reducing payload and battery capacity. To combat this problem, an alternative thrust-vectoring system is desired for an existing vehicle. A number of alternative design strategies and concepts are explored herein. One design concept is then chosen and feasibility calculations are performed. Analysis of hydrodynamic loading, actuators, bearings, and structural components is conducted. The design is then reviewed and improvements are suggested.

Thesis Supervisor: Amos G. Winter
Title: Postdoctoral Research Associate, MIT-SUTD International Design Center

ACKNOWLEDGEMENTS

I would like to acknowledge several people who were indispensible to the completion of this project. First, I would like to thank my thesis supervisor, Amos Winter, who provided me with critical guidance and advice throughout the project. I would also like to thank Jakob Schmidt and the rest of the Bluefin Robotics Corporation for providing a challenging problem, help with brainstorming, and technical information. I also owe many thanks to Emily Tow for being a constant source of thesis-related information, Bayley Wang for his computing hardware, Duncan Townsend for his help with recovering my computer, Laura Royden for her moral support, and Rebecca Colby for ensuring that I continue to eat and sleep. Without the assistance of these people, this project would not have happened.

TABLE OF CONTENTS

LIST OF FIGURES

Figure 4.3.6: Hertzian contact normalized von Mises Stress versus normalize depth in the spherical housing and ball transfers. 62

LIST OF TABLES

1. INTRODUCTION

This work exists primarily as a conceptual study for alternative designs to an existing thrust vectoring tailcone, currently in use on the Bluefin-21 Autonomous Underwater Vehicle (AUV), produced by Bluefin Robotics Corporation. Thrust vectoring redirects thrust for directional control of a vehicle, as opposed to using control surfaces to redirect the external flow. Figure 1.1 illustrates this principle.

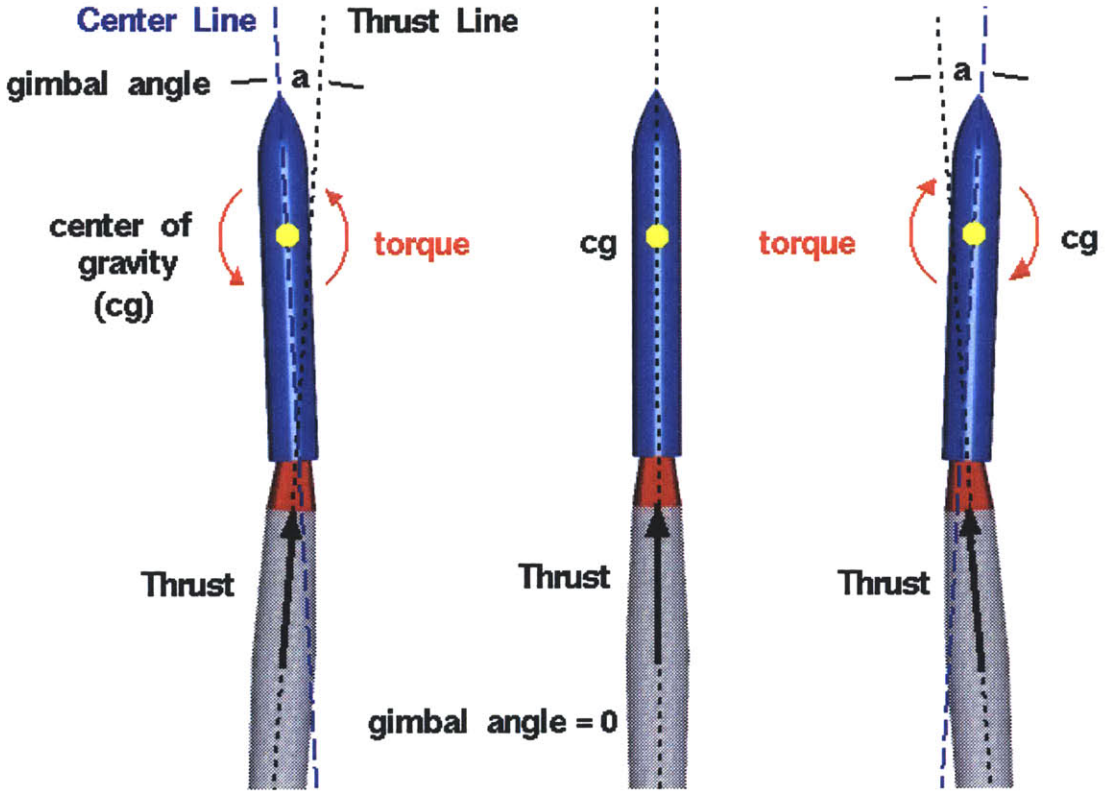

Figure 1.1: Thrust vectoring, applied here to a rocket, can be used on an AUV as an alternative to control surfaces **(1)**.

The Bluefin-21, shown in Figure 1.2, uses a ducted propeller on a two degree of freedom gimbal for propulsion and directional control (herein referred to as the tailcone). This configuration was chosen over a simpler control surface scheme due to the reduced turning radius made possible by thrust vectoring. Unfortunately, the current configuration occupies a relatively large portion of the vehicle's internal volume. If the volume occupied by the tailcone

assembly is reduced, the vehicle can carry additional batteries or payload, improving overall mission capability.

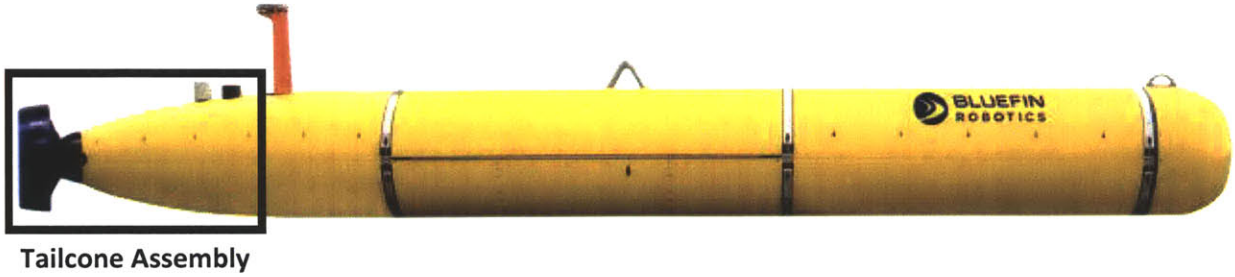

Figure 1.2: Bluefin-21 AUV. The approximate volume occupied by the current tailcone is shown **(2)**.

The goal of this design study was to explore alternative tailcone actuation schemes which could significantly reduce the volume occupied by the system. A number of concepts were proposed and qualitatively assessed. A single concept was then chosen and a first-order feasibility analysis was performed. The analysis included component packaging, actuator specification, bearing sizing, and stress analysis. A first-order hydrodynamic analysis was also conducted to estimate external loads on the system.

2. DESIGN APPROACH

2.1. Design Specifications

A set of Bluefin specified design requirements for the new 21" tailcone are listed in Table 2.1.1 below.

Table 2.1.1: Design requirements for Bluefin-21 Tailcone

Design Requirement	Specification
Size	Shorter than 21"; smallest possible design preferred
Propulsion power	1-2 kW
Noise	Minimal
Actuation range	+/- 15° pitch and yaw
Actuation speed	30°/second
Actuation frequency	+/- 1° at 5 Hz
Vehicle speed	6 Knots
Operating temperature	-20 to 122 °F
Power Supply	60 V @ 40-50 A max.
Hydrodynamics	Minimal modification to current configuration

2.2. Design Considerations

The primary requirements focused on in this design study were size, actuation characteristics, and hydrodynamic modification. Vehicle speed manifested itself in loading, and therefore component sizing; however, propulsion, power supply, operating temperature, and noise remained secondary in concept assessment. Electrical power supply requirements were taken as flexible, since voltage can easily be regulated; as such, voltages were largely ignored. Additionally, temperature restrictions were regarded as being a factor in detailed materials choice and control electronics, and were also largely ignored.

Noise and propulsion power were considered in more detail. In the current tailcone design, shown in Figure 2.2.1, the main source of noise is the propulsion gearmotor. Consequently, all proposed design concepts assumed a direct-drive motor for propulsion. Based on propeller performance, a motor capable of 24.5 N-m of torque at 600 rpm (1.5 kW) is required. Specifications for a possible propulsion motor are given in Table 2.2.1. Though the

sample motor figures are non-ideal for this application, they are simply used for reference: the ideal motor will have similar performance, and since electric motor performance is dictated by thermal and electrical geometry, similar size. The propulsion motor is therefore assumed to be of nine inch diameter and three inch length for all design concepts, based on the motor presented in Table 2.2.1. Detailed propulsion motor selection is deferred to future development efforts.

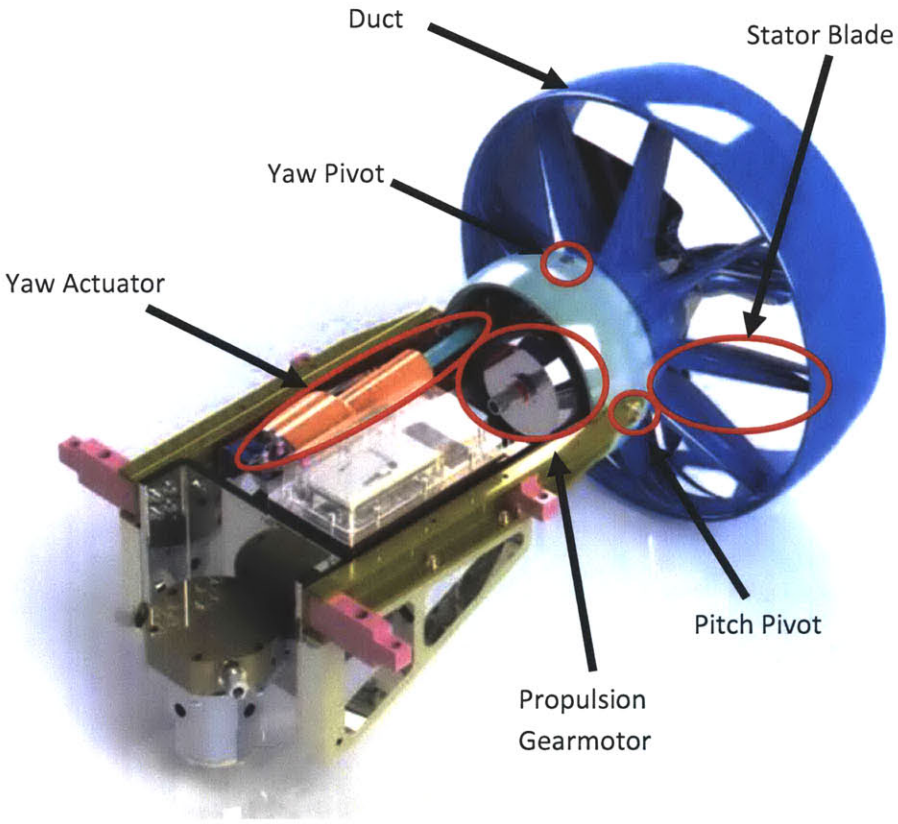

Figure 2.2.1: A rendering of the current Bluefin-21 tailcone, with gearmotor, yaw and pitch pivot points, yaw actuator, duct, and stator labeled.

Table 2.2.1: Sample propulsion motor specifications for Aerotech, Inc S Series Brushless, Frameless Torque Motor. It is evident from these specifications that a motor of these dimensions could provide the requisite performance **(3)**

Motor Model	**Units**	**S-240-43**
Winding Designation		**B**
Performance Specifications		
Stall Torque, Continuous	N·m	10.73
Peak Torque	N·m	42.90
Rated Speed	rpm	1200
Power Output, Continuous	W	1347.9
Length of Winding, Frameless Motor	mm	42.7
Outside Diameter, Frameless Motor	mm	239.2
Rotor Bore Diameter	mm	120.6

A direct-drive motor, while providing substantially reduced noise and part count, introduces a geometric constraint: in the existing Bluefin tailcone designs, the gearmotor is mounted on the gimbal and moves with the ducted propeller. This is not easily achievable in a direct-drive configuration, as the motor diameter is too large for reasonable motion to be achieved within the fairing enclosing the tailcone. As such, power must be transmitted from the propulsion motor to the propeller via a flexible shaft joint. Four possible shaft joint designs, shown in Figure 2.2.2a-d, are outlined in Table 2.2.2.

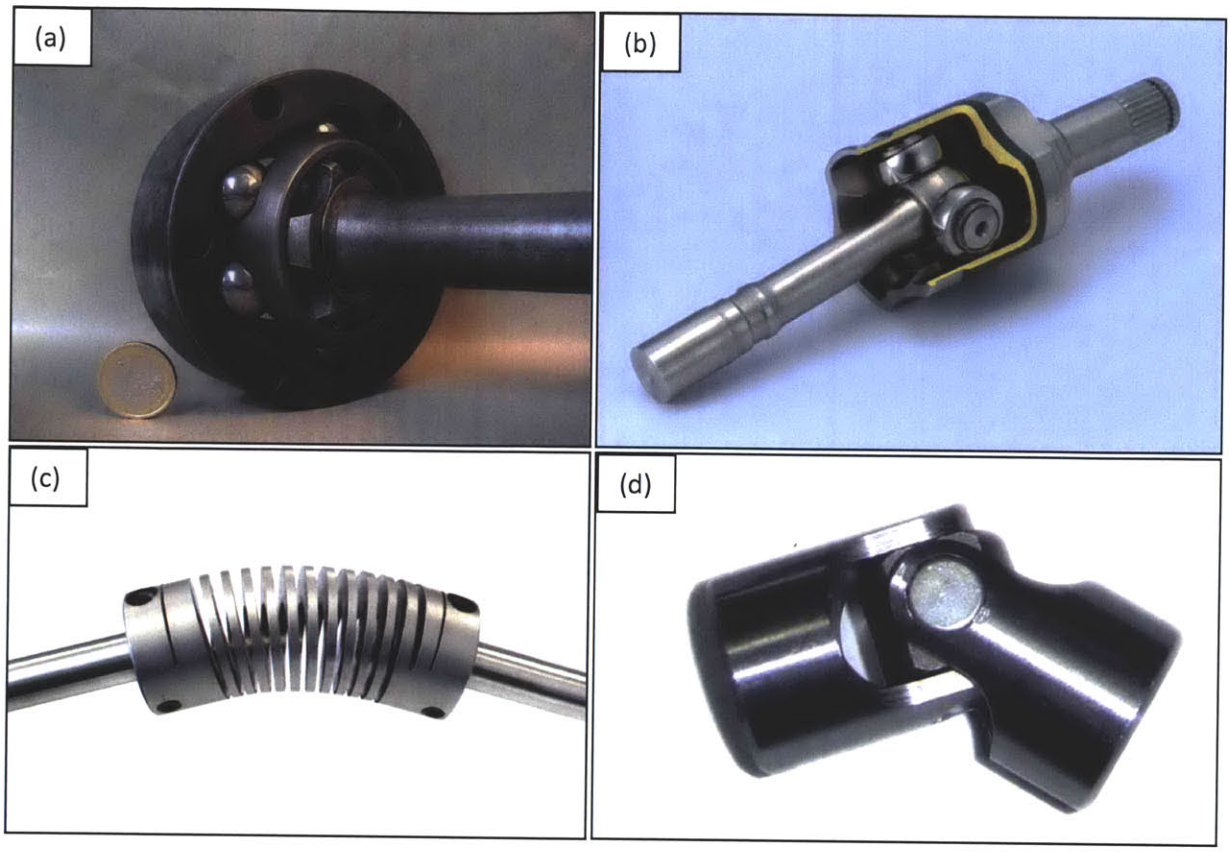

Figure 2.2.2 a: Rzeppa-type **(4) b:** Tripod-type **(5) c:** Flexure-type **(6) d:** U-joint **(7)**

Table 2.2.2: Flexible shaft joint design comparison

Joint Design	Advantages	Disadvantages
Rzeppa joint	• Smooth power transmission • Constant velocity	• Large diameter • Heavy • Loose parts generate noise • Difficult to acquire
Tripod joint	• Smooth power transmission • Constant velocity • Lightweight	• Large Diameter • Potential for noise
Flexure coupling	• Smooth power transmission • Constant Velocity • Lightweight • Low noise	• Elasticity between shaft and propeller • Potential shaft whip problem • Torque required to bend
U-joint	• Lightweight • Easy to implement • Low cost	• Not constant velocity • Noise at large deflection • Potentially harmful vibrations

Rzeppa joints, most commonly used in automotive applications, were immediately eliminated. Commonly available Rzeppa joints are sized and built for high-power and high-torque applications, so off the shelf Rzeppa joints are exceedingly large and heavy. Additionally, the ball bearings used for motion coupling tend to generate excessive noise. U-joints were also quickly eliminated, as they are prone to excessive noise and vibration at large angles of deflection, due to their non-conjugate action. Of the remaining options, flexible couplings are perhaps the simplest solution; however, the couplings rely on deformation, so their behavior at large deflections may be unpredictable. This deformable nature could potentially lead to shaft-whip and fatigue problems. The deformation also creates an increasing force with increasing deflection, demanding additional work from the actuators. Regardless, the option is an entirely viable solution, and all designs presented herein could be adapted to work with said coupling.

Consequently, the tripod joint was selected for shaft power transmission. The behavior of the tripod joint is very predictable, and a reasonably lightweight and compact version is available through Taylor Race Engineering, as shown in Figure 2.2.3.

Figure 2.2.3: The Taylor Race Engineering aluminum tripod housing, measuring 84 mm in diameter, 30 mm in width, with a mass of 211 grams, is lightweight and reasonably compact. It is compatible with off-the-shelf tripods, also available through Taylor Race Engineering **(8)**

2.3. Design Strategy

Three design strategies were originally consider for reducing the size of the existing tailcone:

- Integrate actuation and propulsion into one motor
- Move to an external actuation system
- Move the pivot point to center of pressure

The first strategy would involve the implementation of a spherical motor: a motor that can rotate continuously about its primary axis while being able to move the primary axis in two degrees of freedom. Such motors have been the subject of research for decades, but none are available commercially, and the idea was ruled out due to feasibility issues.

The second strategy involved externalizing the yaw and pitch actuators to increase available internal volume. However, the strategy was quickly eliminated, as it would interfere significantly with the hydrodynamics of the vehicle. Additionally, the actuators would be exposed to external impact, which would make the AUV very susceptible to damage.

The strategy of moving the pivot point to the center of pressure was thus adopted. Lift and drag on an object moving through a fluid are generated by pressure distributions over the objects surface. The integral of the pressure over the surface gives the resulting forces; those forces can be thought of as acting through a single point on the body. The point through which these forces act is called the center of pressure, and no moments are generated around that point. If a lifting body is held aft of the center of pressure, the body will pitch up; if the body is held fore of the center of pressure, it will pitch down. Therefore, placing the pivot point of the tailcone assembly at the center of pressure of the ducted propeller would generate no pitching moment, and the required actuators would become substantially smaller.

3. DESIGN CONCEPTS

3.1. First-Order Duct Force Calculations

Before meaningful design concepts could be generated, the center of pressure of the ducted propeller assembly needed to be estimated. Fletcher presents experimental results for lift, drag, and pitching moment of five ring airfoils in non-axial flow in NACA Technical Note 4117 (9). The ducts were revolutions of the Clark-Y airfoil profile with chordline at zero angle of attack. The results are presented based on the conventions shown in Figure 3.1.1.

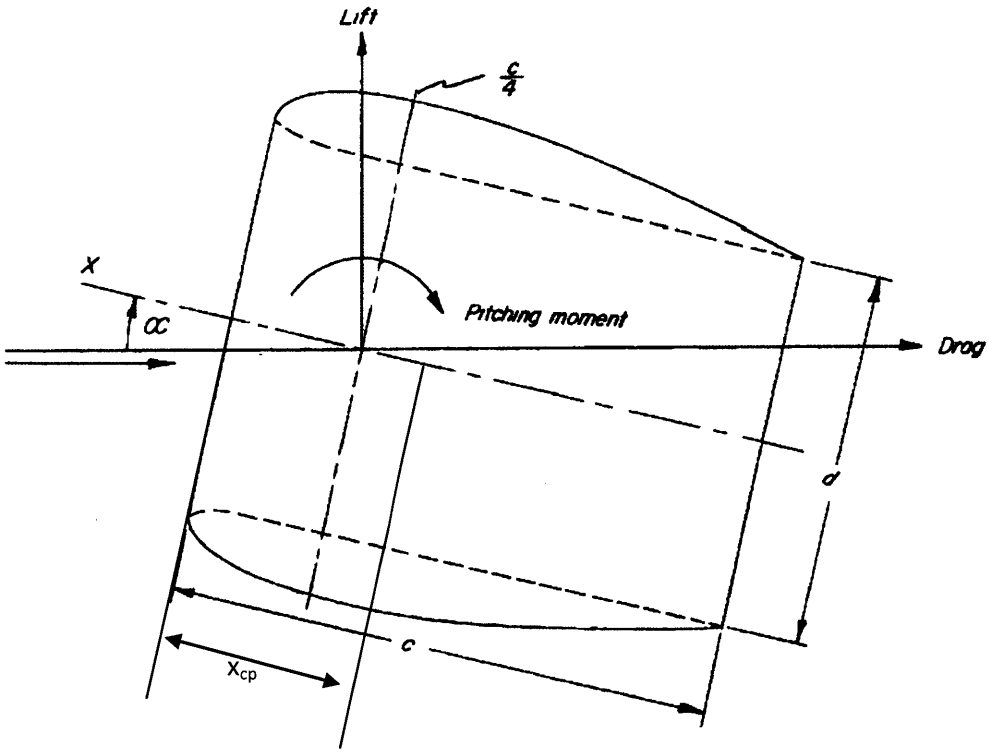

Figure 3.1.1: Convention for lift, drag, and moment on a ring airfoil/duct. Chord is given by c, inner diameter is given by d, center of pressure distance from leading edge is x_{cp} and angle of attack is given by α. Moments are taken around the quarter chord point. Lift is taken as normal to the flow, not the duct. **(9)**

Fletcher gives the non-dimensional center of pressure as a fraction of the chord length, and presents the results for five different aspect ratios, defined by Equation 1, where aspect ratio is A, chord is c, and duct diameter is d.

$$A = \frac{d}{c} \tag{1}$$

For the Bluefin-21 duct, the chord is 0.1239 meters and the diameter is 0.3860 meters, giving an aspect ratio of 3.12. Fletcher's center of pressure results for a duct of aspect ratio equal to 3 are shown in Figure 3.1.2.

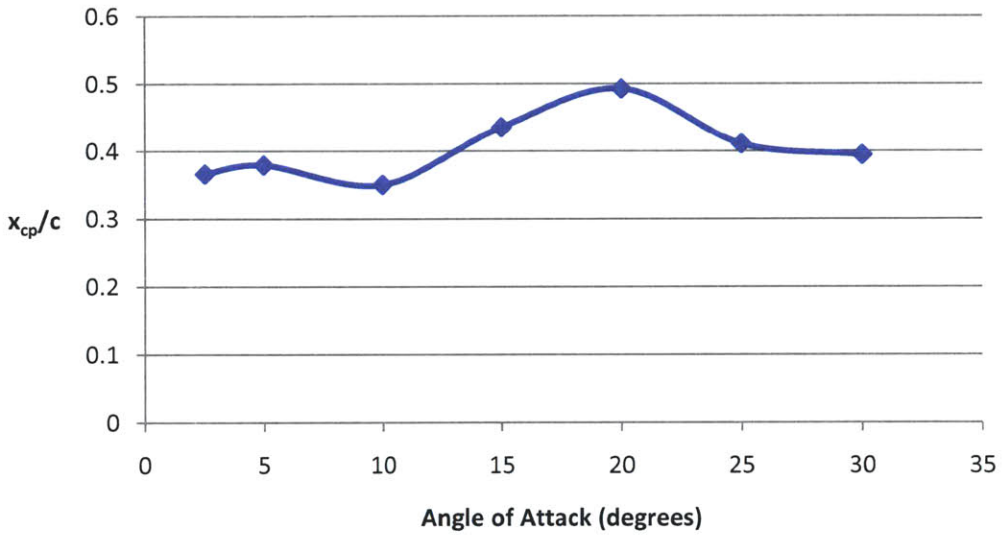

Figure 3.1.2: Non-dimensional center of pressure as a fraction of chord length versus angle of attack for an annular Clark-Y airfoil of aspect ratio 3. **(9)**

Ideally, the pivot point could remain at the center of pressure under all conditions. Unfortunately, as visible in Figure 3.1.2, the center of pressure shifts with change in angle of attack. The hydrodynamic forces also increase with angle of attack, so the pivot location that most easily minimizes forces is at the center of pressure for the worst-case loading: i.e. highest angle of attack seen. In this case, the maximum angle of attack can be taken as fifteen degrees: full actuation in one degree of freedom. At this angle of attack, the center of pressure is at 43.5% of the chord from the leading edge. To first-order, ignoring effects of airfoil profile, airfoil angle of attack, and the duct stator, the center of pressure on the Bluefin-21 duct is approximated as shown in Figure 3.1.3.

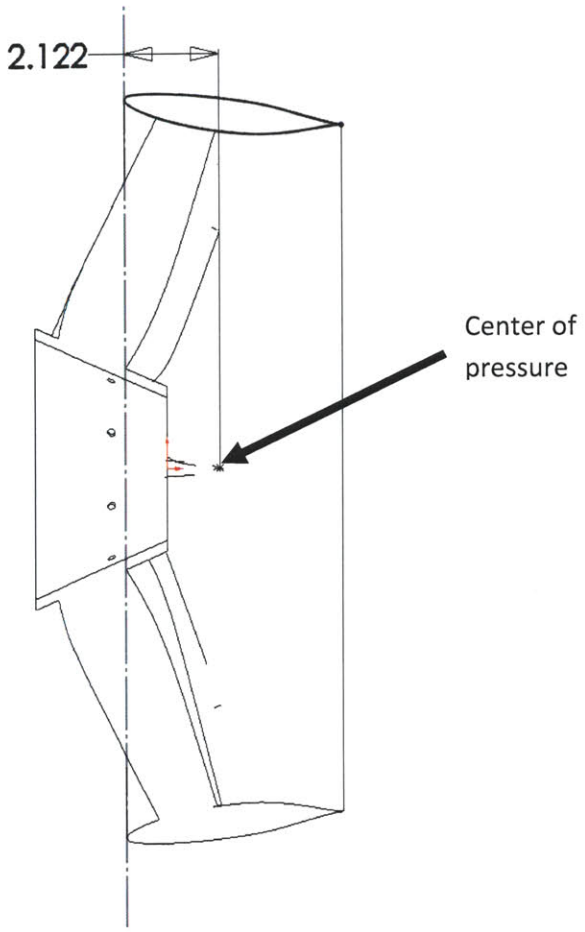

Figure 3.1.3: The first-order estimated location for the center of pressure on the Bluefin-21 duct.

As made apparent from this estimate, the center of pressure is likely to be aft of the duct mounting point and contained within the propeller. As such, creating a pivot point at the center of pressure proves to be challenging: space is limited, and the pivot may have to be enclosed in the rotating housing of the propeller. Moving the pivot point as close to the center of pressure as possible, however, still promotes significant downsizing of actuators. In the current configuration, the pivot point is 6.6 inches from the estimated center of pressure. By moving the pivot to the aft edge of the duct mounting, the pivot-to-center-of-pressure distance would be reduced by 80%, resulting in an 80% reduction in required torque, and thus a significant reduction in tailcone volume. However, placing a pivot point inside the duct is still challenging, for space is very limited.

3.2. Proposed Design Concepts

Three design approaches, outlined in Figure 3.2.1, Figure 3.2.2, and Figure 3.2.3, were considered for moving the pivot point rearward. The first approach simply integrates traditional pivot points into the duct mounting. Another approach utilizes pushrod style controls to allow for parallel, rather than series actuation, and more flexibility in hardware placement. The final approach rotates the duct around a virtual pivot, allowing more ideal pivot placement at the expense of geometric complexity. All three approaches require the propeller shaft's flexible joint be coincident with the pivot point, introducing an additional constraint. Variants of each concept are discussed in Section 3.2.1 through Section 3.2.5.

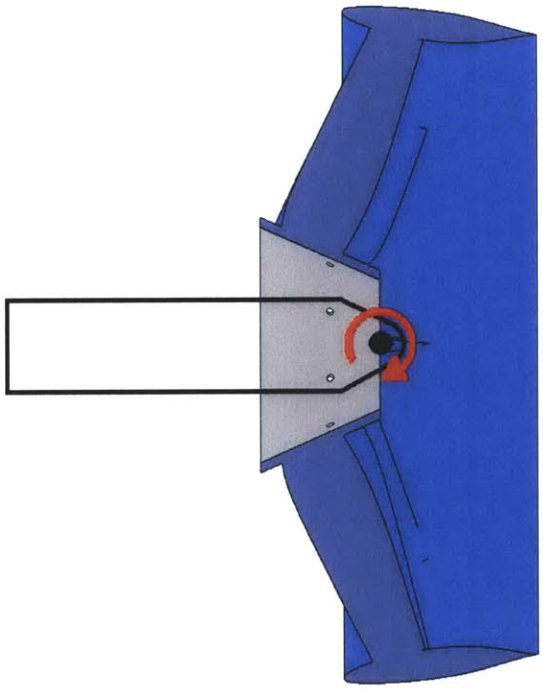

Figure 3.2.1: The direct pivot approach locates a traditional pin-type pivot at the center of pressure. The duct is fastened to the pin and torque is generated by either linear or rotary motors. This concept is similar to the existing system, but with the duct relocated relative to the pivot.

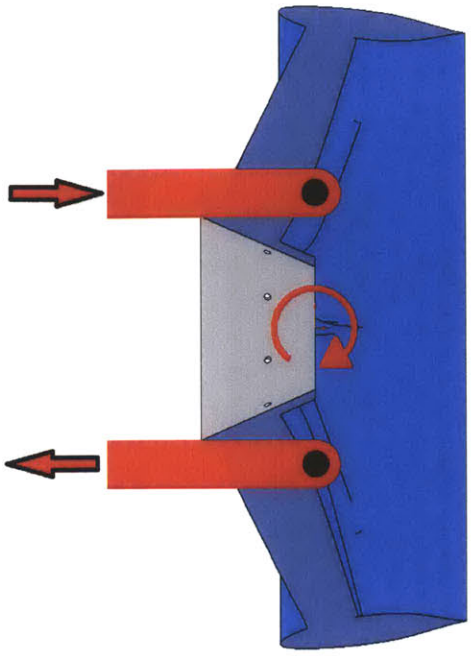

Figure 3.2.2: The pushrod style pivot uses opposing-motion pushrods, mounted external to the duct's pivot point, to create rotation about a point without hardware itself. The pushrods can be mounted anywhere within the plane of the desired pivot.

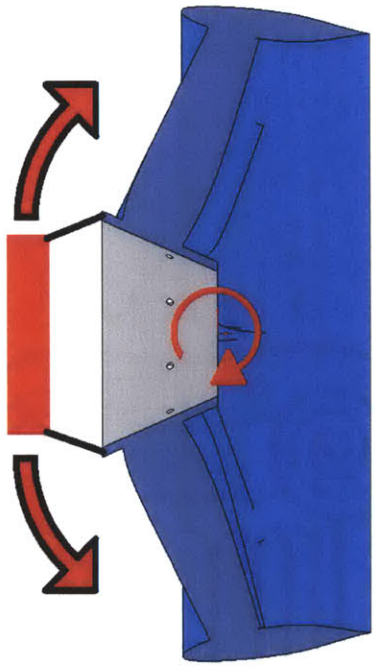

Figure 3.2.3: The floating pivot concept constrains a piece of hardware, mounted external to the duct, to motion in an arc centered at the desired pivot point. The requisite hardware can be mounted anywhere in space, provided its arc of motion is located about the center of pressure.

3.2.1. Direct Pivot Design Concept

The direct pivot design requires two pin-type pivot points be collocated at the center of pressure. A simple gimbal-like design can be used for this, with the propeller-side flexible joint bearing mounted to the outermost gimbal assembly. An illustration of this concept is shown in Figure 3.2.1.1. A direct pivot design can be actuated using linear actuators, similarly to the existing Bluefin-21 tailcone, as shown in Figure 3.2.1.2.

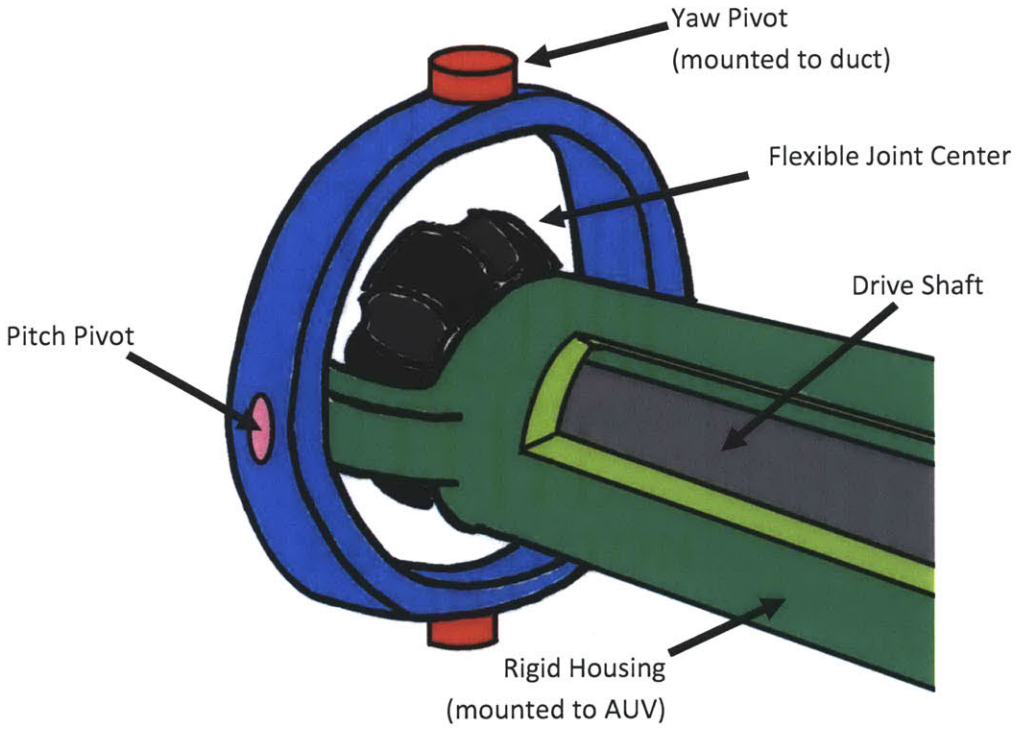

Figure 3.2.1.1: A sample direct pivot gimbal design. The bearing for the flexible shaft joint mounts to the yaw pivot, so as to rotate with the duct.

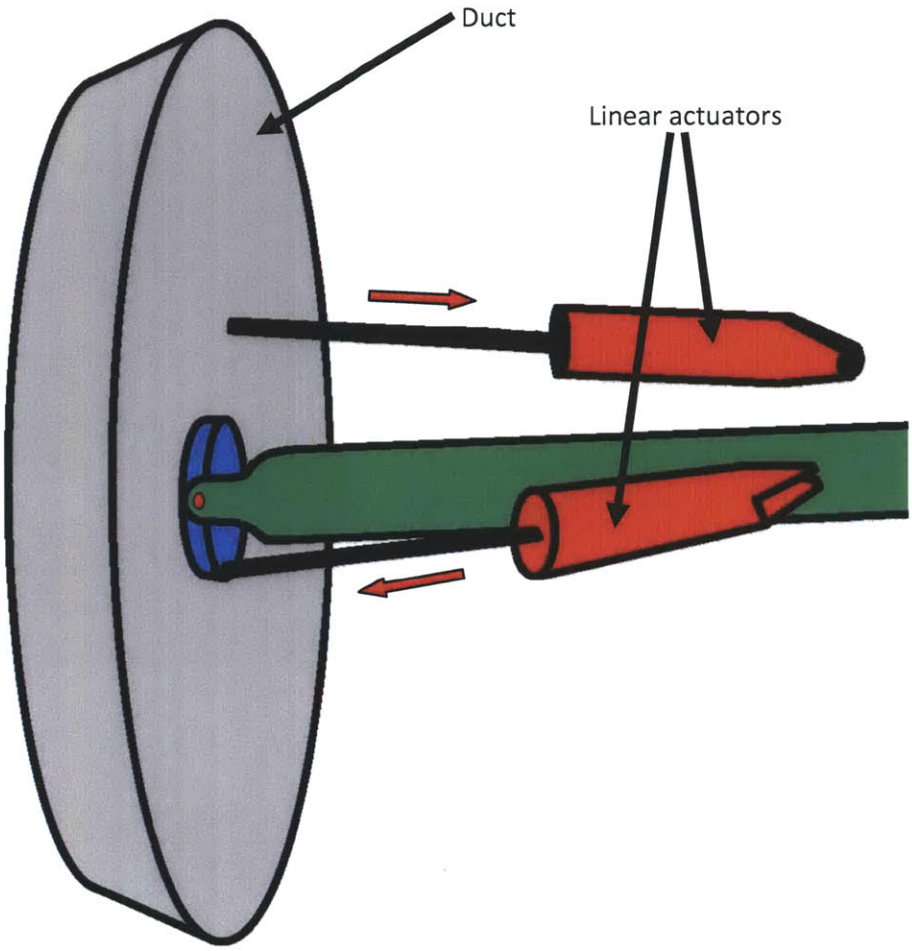

Figure 3.2.1.2: A sample actuation scheme for the direct pivot design, using linear actuators functioning similarly to the current Bluefin-21 tailcone.

The direct pivot design is appealing for its inherent simplicity. The design represents a significant improvement over the existing design; it reduces the required actuator output and shifts the entire assembly approximately six inches aft. A design using rotary actuators could further compact the mechanism, since linear actuators tend to be less space efficient. Unfortunately, this design is not feasible with the current duct and tripod joint, due to limited space within the duct. Figure 3.2.1.3 shows that the suggested tripod joint housing is too large for pivot hardware to be mounted radially to it.

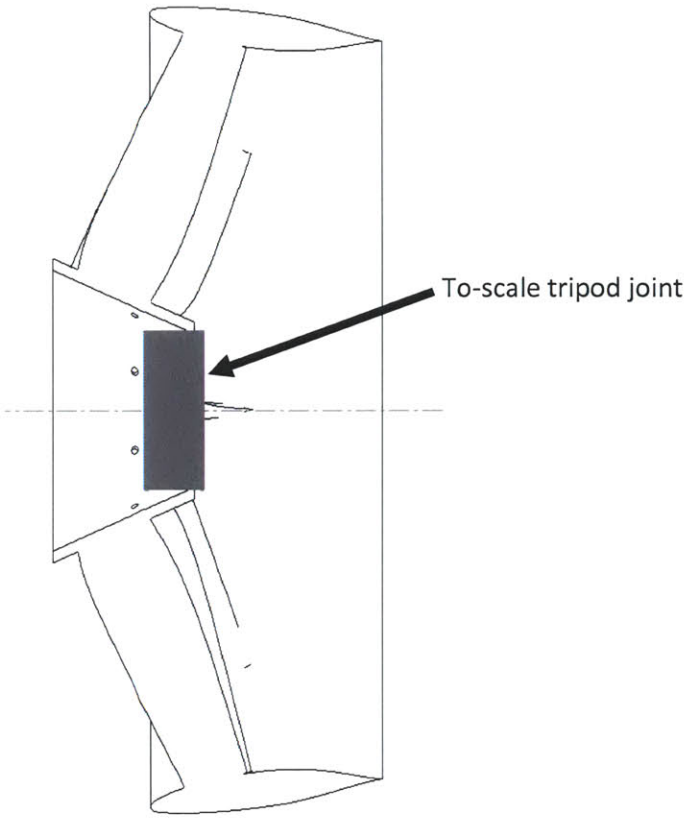

Figure 3.2.1.3: An overlay of the Taylor Race Engineering aluminum tripod housing on the Bluefin-21 duct. It is apparent that very little space is available for coincident pivot point hardware.

While this design can be modified for use with a flexure coupling (thus reducing the required diameter of the gimbal assembly), the additional length and potential shaft whip of such a joint discourage further exploration in this study. This concept is discarded in favor of a more compact design presented in Section 3.2.5.

3.2.2. Pushrod Pivot Design Concept #1

A pushrod style design allows placement of mounting hardware outside the duct, avoiding the limited-internal-volume problem presented in Section 3.2.1. The pushrod design also creates two degrees of freedom through parallel hardware, rather than series hardware (i.e. the yaw pivot does not mount on the pitch pivot, as is done in Figure 3.2.1.1). One pushrod implementation is shown in Figure 3.2.2.1.

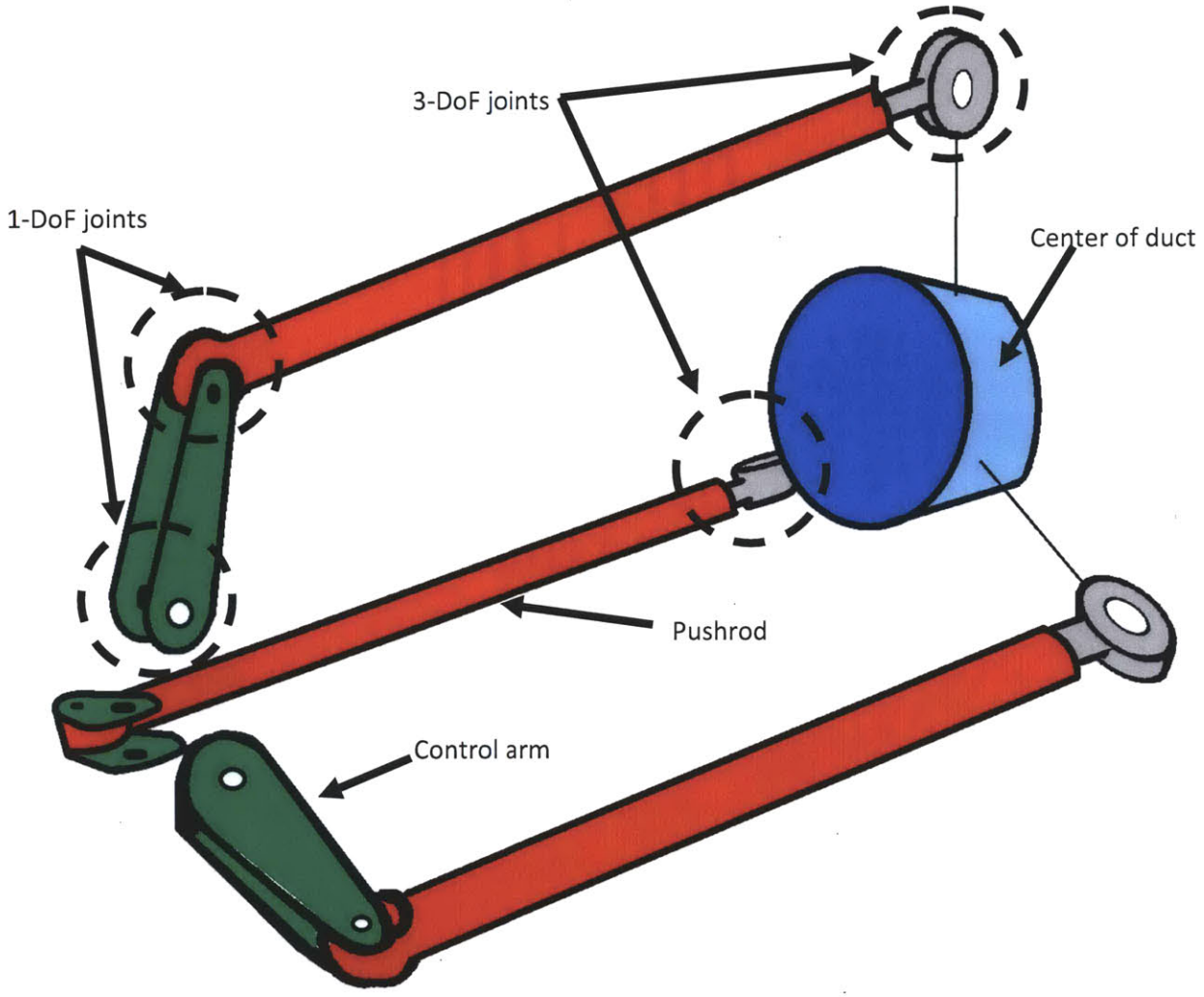

Figure 3.2.2.1: Pushrod concept #1 uses three independently controlled pushrods mounted to the exterior of the duct core. One end of each pushrod features a simple pivot, while the other end features a ball-joint

This implementation uses three independent pushrods, each controlled by a rotary actuator at the base of their control arm. The control arm is affixed to the vehicle by a single degree of freedom pivot, and the pushrod is connected to the other end of the control arm in a similar manner. The pushrods are then connected to the duct via three degree of freedom ball-joints. Accounting for rigid bodies and constraints yields Equation 2.

$$7\ bodies * 6\ DoF - 3\ ball\ joints * 3\ DoF - 6\ pivots * 5\ DoF = 3\ DoF \quad (2)$$

As made apparent in Equation 2, the system is under-constrained. By observation, there are two rotational and one translation degree of freedom. The translational degree of freedom is along the axis of the vehicle, and pure translational motion is achieved when all three pushrods move equally in one direction. As such, the duct needs an axial constraint, or the pushrod actuators need constant power for position-holding during straight-line cruise. Both options are feasible; however, the axial duct constraint adds mechanical complexity, while stalling the actuators requires improved thermal management to avoid runaway heating in the motor windings and eventual failure. As such, and alternative pushrod style design is proposed in Section 3.2.3.

3.2.3. Pushrod Pivot Design Concept #2

A modified version of the pushrod concept presented in Section 3.2.2 is shown in Figure 3.2.3.1. By linking two of the pushrods to the same control arm, one rigid body (six degrees of freedom) and one pivot constraint (five constraints) are eliminated, yielding one less degree of freedom. Consequently, the axial motion of the duct is eliminated, removing the additional mechanical complexity of an axial duct constraint. This design also eliminates the need for actuators to be under constant power, easing thermal design. However, for the pushrod ball-joints to be mounted in-plane with the desired pivot point, they must severely interfere with the hydrodynamics of the duct. The pushrod style design is therefore discarded in this study.

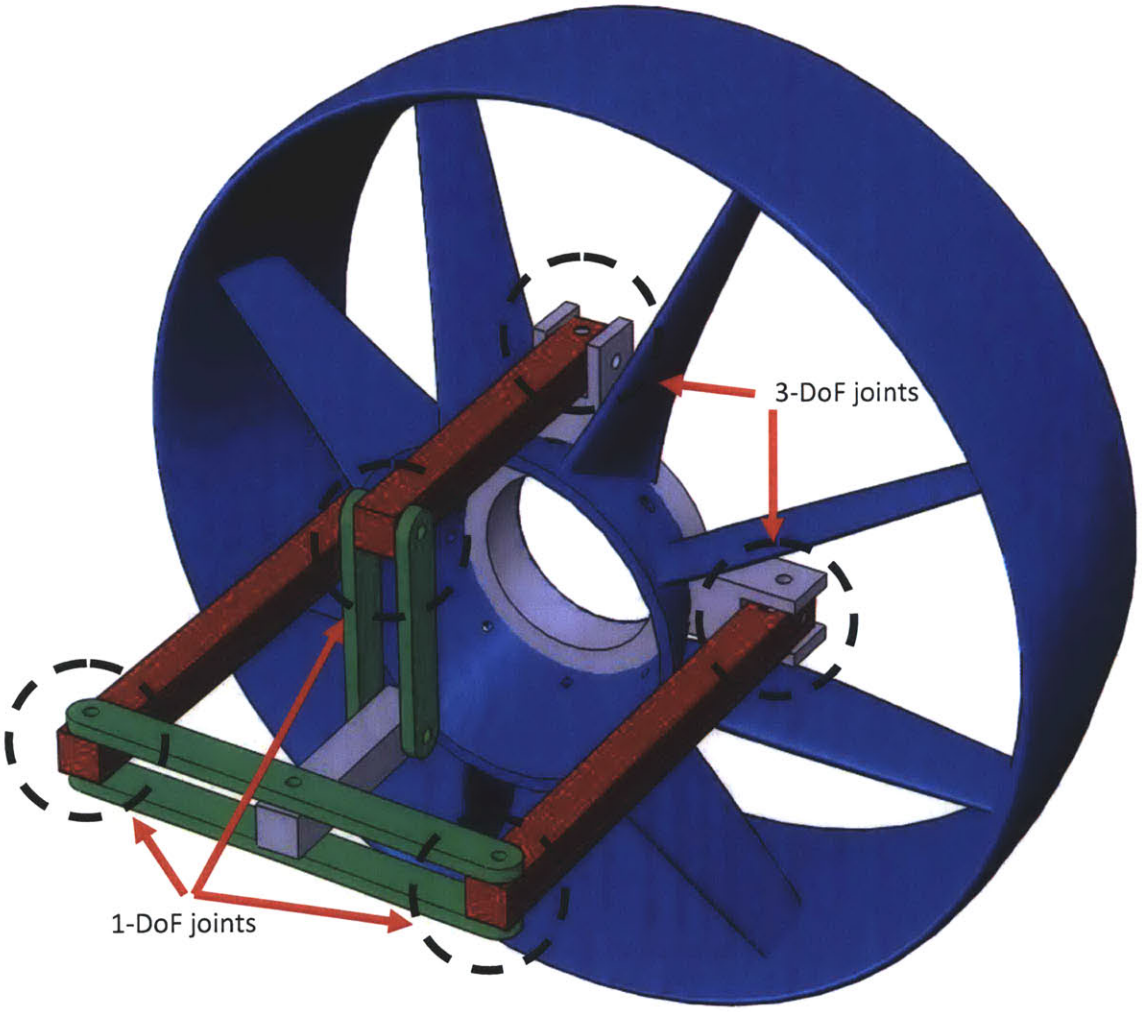

Figure 3.2.3.1: A variation of the pushrod style design presented in Section 3.2.2. By coupling two pushrods to one control arm, the axial degree of freedom is eliminated.

3.2.4. Floating Pivot Design Concept #1

A floating pivot design benefits from remote mounting of hardware: possibly eliminating hydrodynamic interference, avoiding volume limitations within the duct, and enabling placement of the pivot closer to the center of pressure. One method for achieving a floating pivot is by use of an asymmetric four-bar linkage, as illustrated in Figure 3.2.4.1. While the portion of the linkage connected to the duct does not move along an exact arc, the spatial deviation of the "pivot point" is small enough to be accommodated by the flexure coupling or tripod joint.

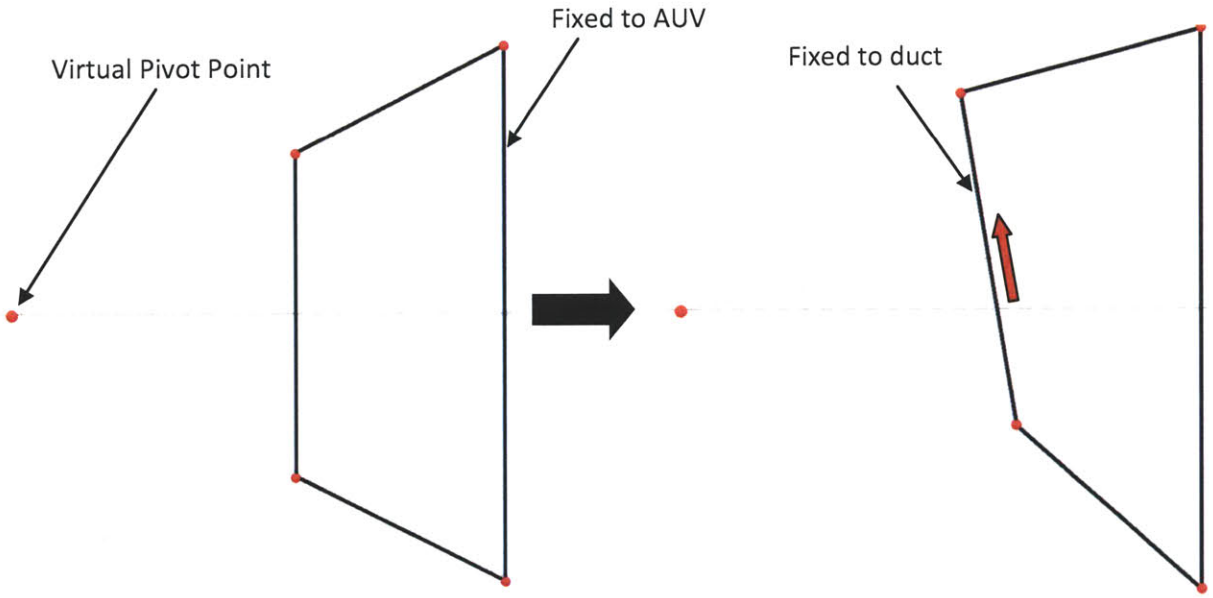

Figure 3.2.4.1: Asymmetric four-bar linkage that achieves virtual pivot point. The virtual pivot point moves slightly axially and radially.

This two dimensional concept is adapted into a three dimensional concept illustrated in Figure 3.2.4.2. In this concept, four connecting rods are affixed to the AUV by ball-joints with three rotational degrees of freedom. The duct is mounted to the opposite end of the connecting rods using joints with two rotational degrees of freedom, similar to a u-joint. Accounting for rigid bodies and constraints yields Equation 3.

$$5\ bodies * 6\ DoF - 4\ ball\ joints * 3\ DoF - 4\ u\ joints * 4\ DoF = 2\ DoF \qquad (3)$$

This suggests that the linkage will create the necessary degrees of freedom, assuming no redundant constraints are present. Linear actuators could likely be implemented in the manner shown, with a ball-joint on one end, and a u-joint on the other end. Two actuators would introduce twelve degrees of freedom and fourteen constraints, resulting in a perfectly constrained system for a given actuator position. This design benefits from remote placement of mounting hardware (i.e. the location of the pivot point does not dictate the location of the linkage joints). However, the design requires a reasonable volume forward of the duct for actuation, and linear servo actuators are generally less space efficient than an equivalent rotary motor. Additionally, the axial and radial motion of the virtual pivot point is less than ideal. For these reasons, the design presented in Section 3.2.5 is pursued instead.

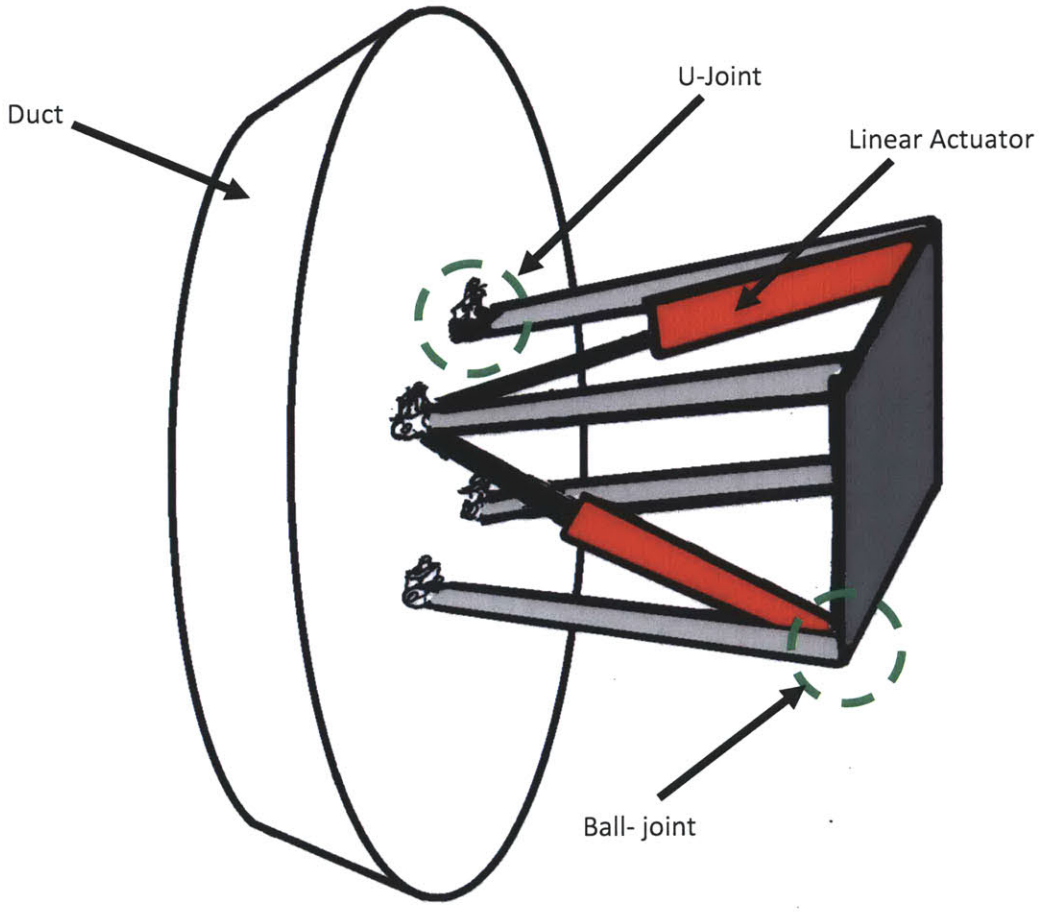

Figure 3.2.4.2: Possible implementation of asymmetric four bar floating pivot concept. Duct-side joints are two degree of freedom u-joints, AUV-side joints are three degree of freedom ball-joints.

3.2.5. Floating Pivot Design Concept #2

To achieve ideal pivot placement and minimum volume, the design illustrated in Figure 3.2.5.1 through Figure 3.2.5.3 was chosen. The design utilizes four ball transfers (load bearing balls that can rotate in two directions) on a spherical surface to constrain the duct to motion around the center of the sphere. Each ball transfer can only exert a radial force, because two spheres theoretically only contact at a single point. As such, each ball transfer acts as a single translational constraint. However, the ball transfers can only generate a positive force; otherwise separation of the surfaces will occur. For this reason, an extra ball transfer is needed to generate three translational constraints. This leaves the duct with three rotational degrees of freedom about the center of the sphere. The remaining rotational degree of freedom is dealt with through the gear train, discussed later.

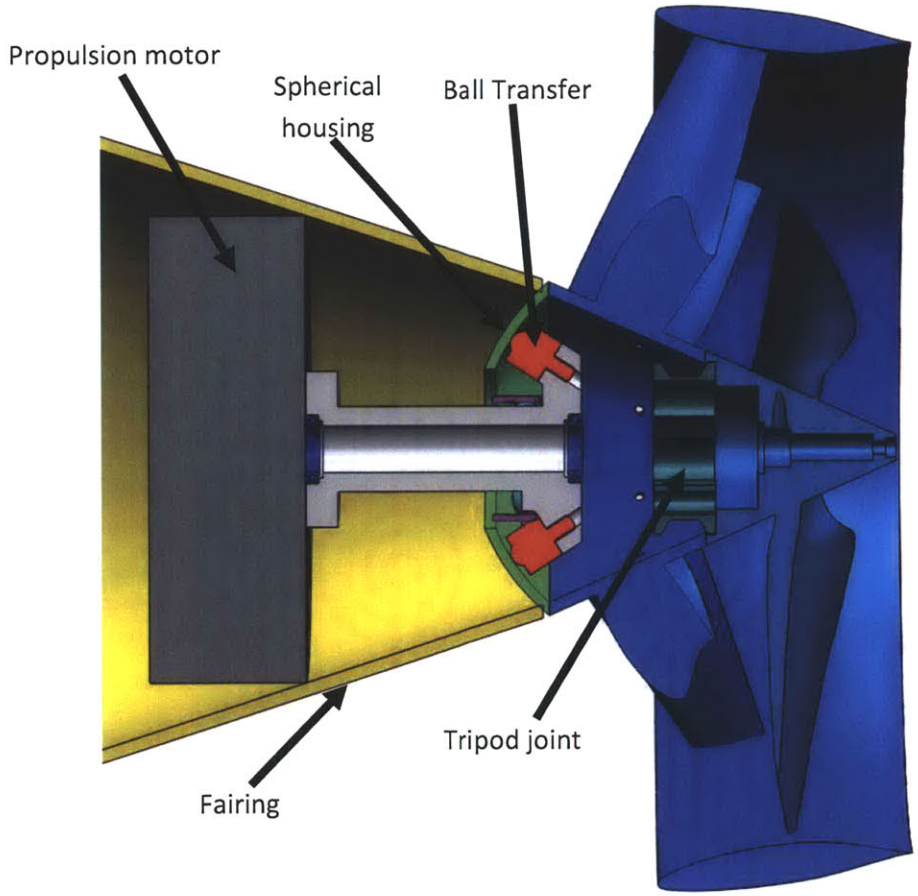

Figure 3.2.5.1: A cross-sectional side view of the spherical floating pivot design. Note that the propulsion motor limits the minimum length of the assembly. A smaller diameter motor shortens the entire system.

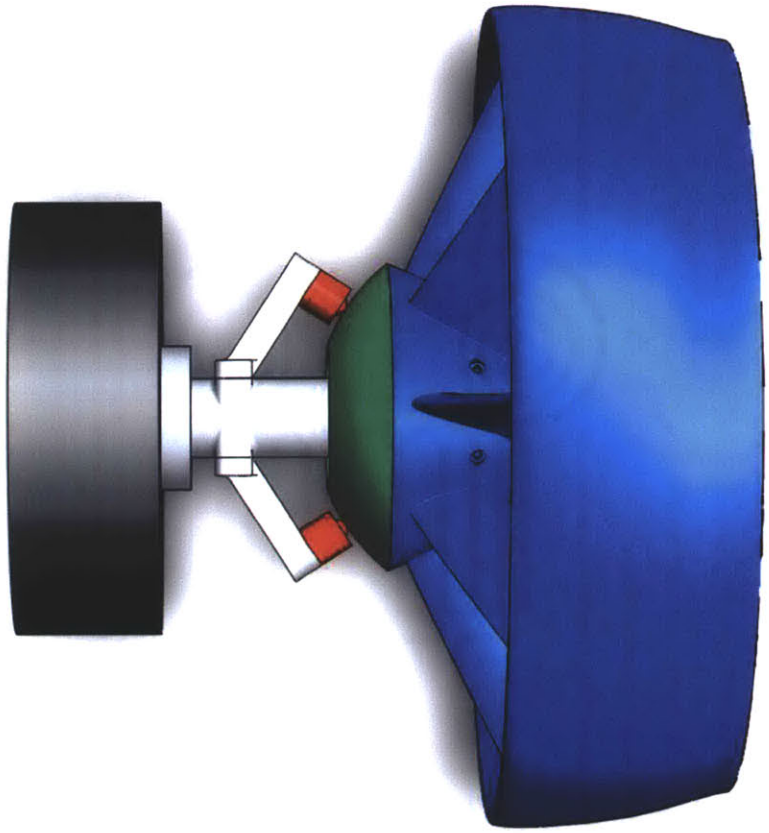

Figure 3.2.5.2: Top view of the spherical floating pivot design. Note that the exterior ball transfers are located in an orthogonal plane to those inside of the spherical housing. This is done to properly constrain the duct.

The spherical shell utilizes very little space, allowing the actuation system to be placed within duct. Thus, the drive motor is the limiting factor in total system volume, as it needs to be enclosed within the vehicle fairing (as seen in Figure 3.2.5.1). Consequently, this design is appealing when maximizing vehicle payload.

The drive system, shown in Figure 3.2.5.3, utilizes two gear stages in series. The actuator controlling yaw is mounted to the primary support beam and drives a floating gear assembly. The pitch actuator is mounted to the floating yaw-gear assembly. This actuator drives the pitch-gear assembly, mounted rigidly to the duct. The pitch-gear assembly floats on the yaw-gear assembly using a similar mechanism as the yaw-gear assembly on the primary support beam.

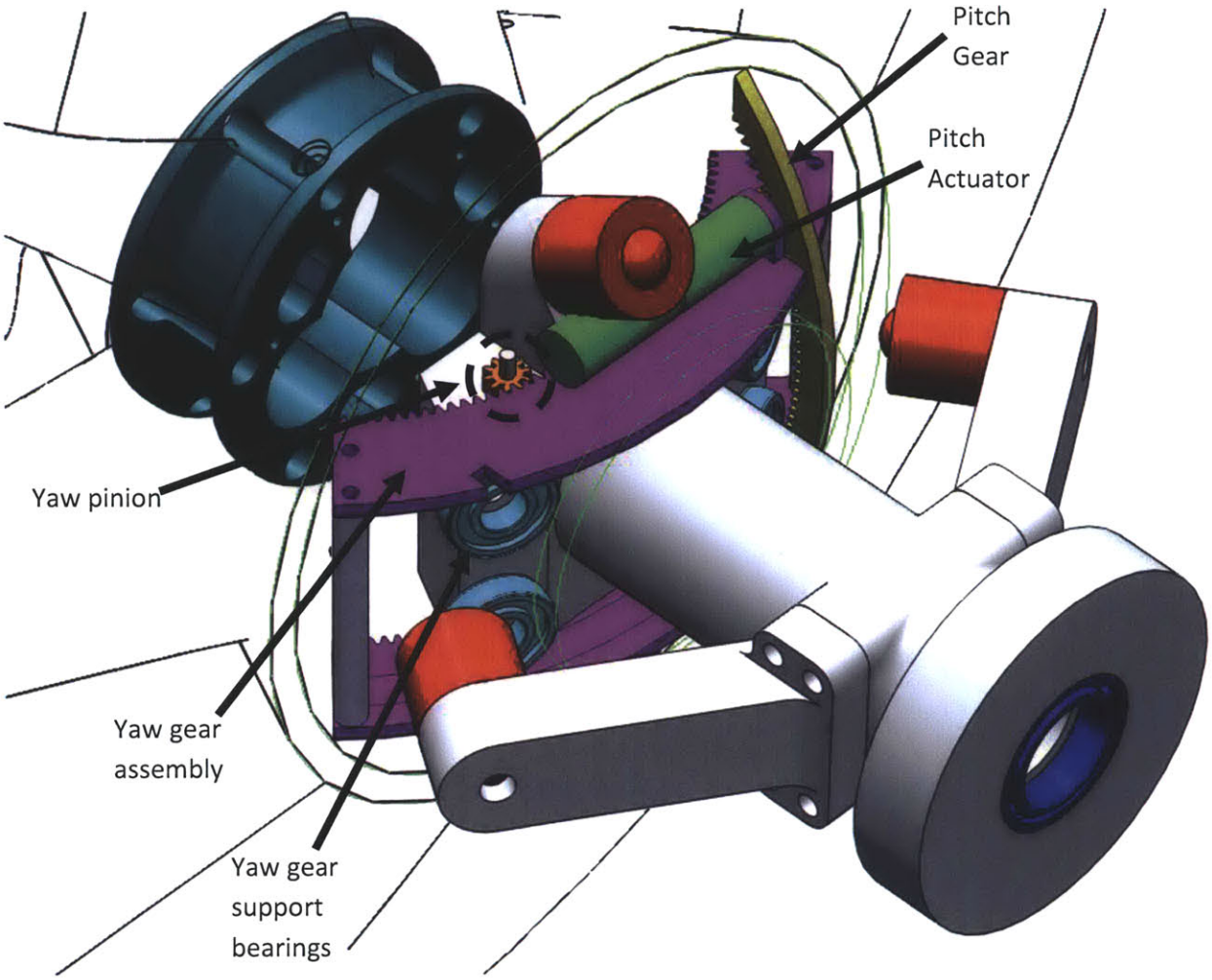

Figure 3.2.5.3: A view of the spherical floating pivot drive system. Note that there is adequate clearance between the yaw gear support bearings and the pitch gear, as well as the inner ball transfer and the pitch actuator. The pitch gear and propeller bearings, as well as the drive shaft and propulsion motor are not shown here.

A more detailed view of the floating yaw gear assembly is presented in Figure 3.2.5.4 and Figure 3.2.5.5. The two gears of the assembly sandwich a set of four bearings, which sit in concave troughs that form an arc centered at the pivot. The surface of the bearings is spherical, creating point-contacts that allow the cylindrical bearings to sit in the trough without jamming. The axes of the bearings are aligned radially to the axis of the floating gear assembly to permit arc-like motion. If the gear assembly attempts to move in any direction other than the prescribed

arc, the bearings attempt to lift out of the trough, forcing the separation of the gear assembly; however, this is not possible.

Each bearing provides two constraints: a normal force (radial to the bearing) and a retaining force keeping the bearing from moving in the trough (axial to the bearing). Since the bearings can only provide a positive normal force (else the surfaces would separate), a complementary bearing is required. It can thus be seen that three bearings (two along the upper trough, one along the bottom trough) would constrain the assembly to one degree of freedom. However, four bearings are used instead to reduce the radial load seen by an individual bearing when a torque is applied about the axis of the propulsion motor (described in Section 4.3). The floating yaw-gear is also coupled to the adequately constrained duct. While the yaw and pitch-gear assemblies prevent rotation about the axis of the duct, they introduce redundant constraints. To prevent over-constraining the system, loose tolerances should be held on the floating gear assemblies. The support bearings should only see loads from moments around the axis of the duct, and forces transmitted through the actuators. As will be shown in Section 4.3, these forces prove to be substantially lower than those seen by the ball transfers.

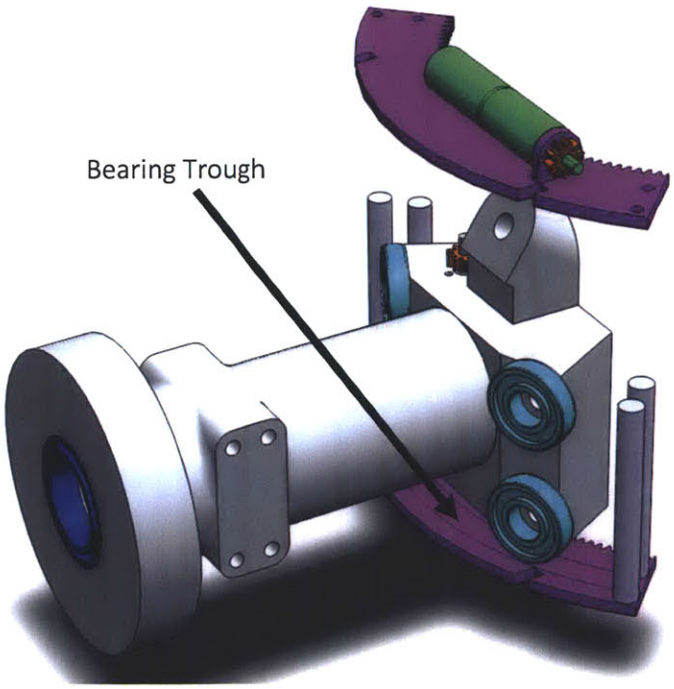

Figure 3.2.5.4: An exploded view of the primary support beam and floating yaw-gear assembly.

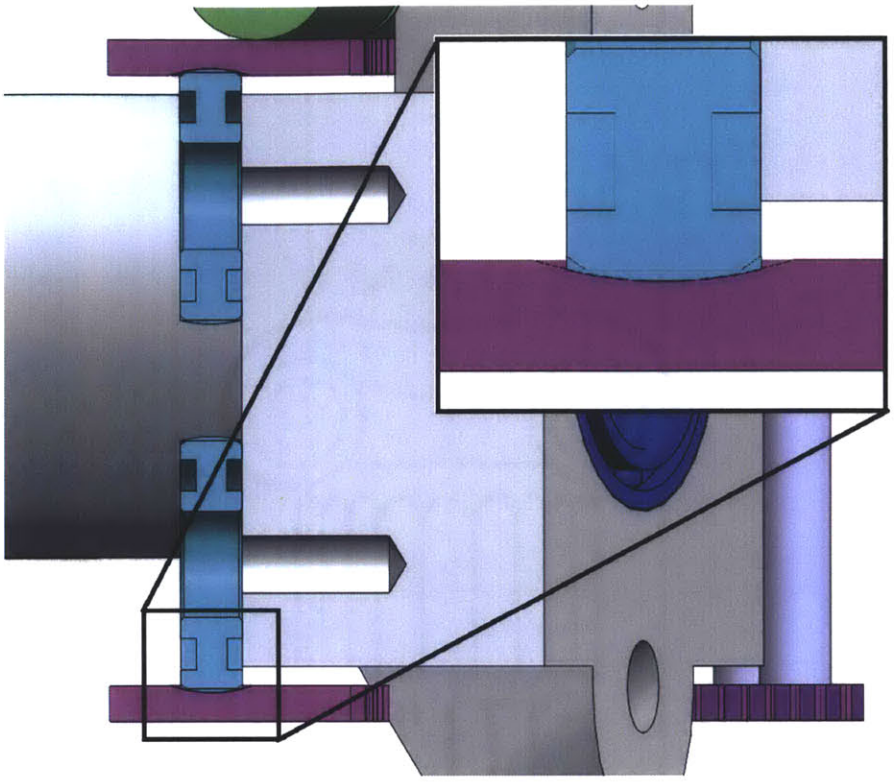

Figure 3.2.5.5: A detailed view of a support bearing in its trough. The radii of the surfaces can be adjusted to minimize rubbing.

This design is analyzed in Section 4 and evaluated in Section 5. However, it is worth noting now that the maximum travel of the duct was reduced from +/- 15 degrees to +/- 10 degrees in the designs presented. This was done to avoid modification to the duct, given the center of pressure found by the procedure outlined in Section 4.1. An error in this procedure suggested the center of pressure to be further aft, and the spherical floating pivot design geometry was based on this assumption. The calculations were corrected, but due to time constraints, the geometry of the design could not be changed. Since the center of pressure was found to be further forward, this design can be modified to give the requisite travel, or an alternative design could be pursued (e.g. direct pivot).

4. DESIGN ANALYSIS

To assess the feasibility of the spherical floating pivot design, a general analysis of all critical components was done. Actuator options were investigated to assess the possibility for packaging actuation within the duct. A more refined hydrodynamic assessment was then conducted to better analyze the loading on actuators, bearings, and other components. The loading of components under static conditions was then calculated, and lifetime estimates were made where possible.

4.1. Moment Estimation and Actuator Motor Selection

For first-order approximation of the required actuator size, a basic model is needed for moments about the chosen pivot. The four primary causes of moments about the pivot are:

- Lift and drag from the duct at a given angle of attack
- Lift and drag from the duct stator at a given angle of attack
- Drag created by sweeping the duct radially through the water
- Gyroscopic forces from the propellers
- External impact

These contributions (excluding impact) are analyzed at full travel in one dimension (e.g. 15 degrees yaw) at full speed (3 m/s) at full actuation rate (30 degrees/sec).

For a sufficient estimate of duct forces to be made, a more accurate prediction of the center of pressure must be made. The center of pressure of an aerodynamic body is heavily influenced by its shape, as the pressure distribution over the surface determines its location. The total momentum change of the incoming flow determines lift and drag forces, which may be identical between ducts of similar dimensions and aspect ratios: however, the manner in which the flow is turned, and thus the location where the forces can be said to act (i.e. center of pressure) varies largely based on airfoil profile and airfoil angle of attack relative to the duct's axis. Figure 4.1.1 shows the profile variation between the Bluefin-21 duct and the Clark-Y duct Fletcher uses in his characterization of ducts.

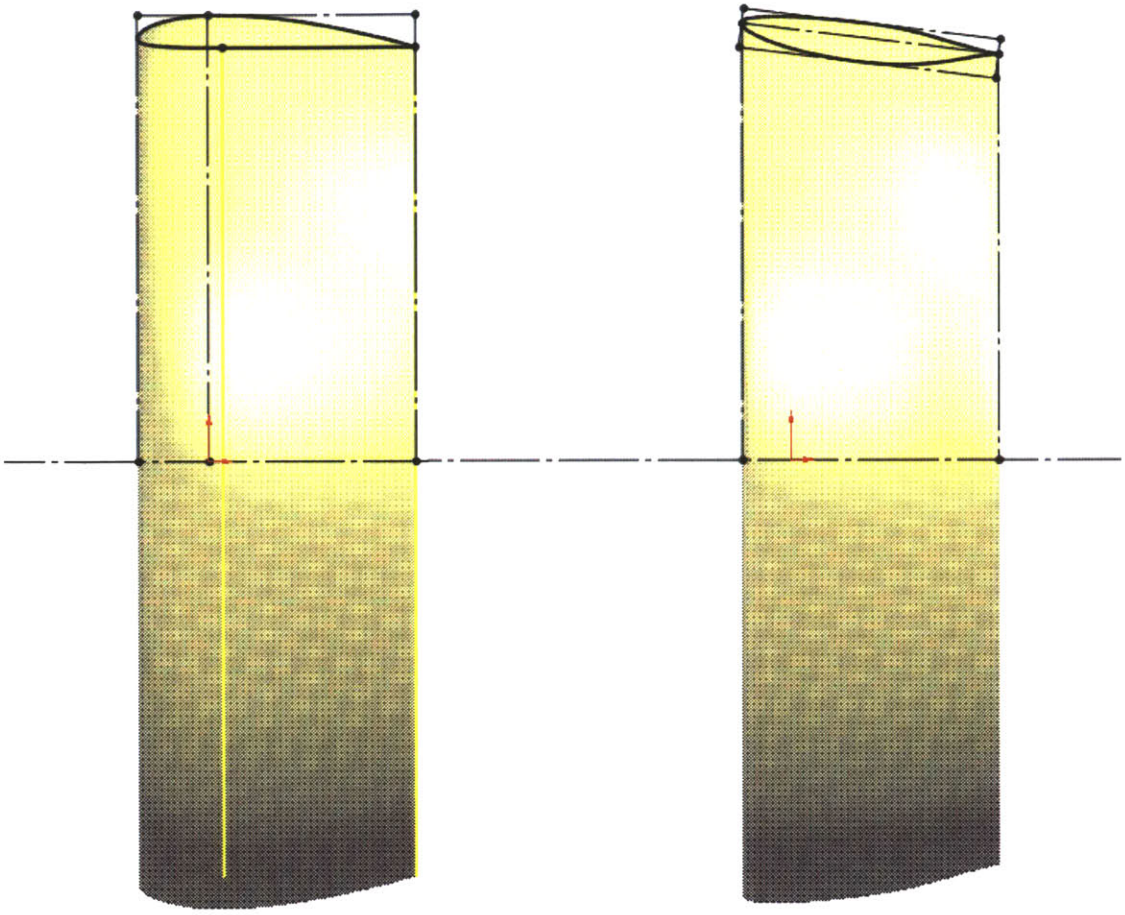

Figure 4.1.1: The Bluefin-21 duct, shown on the right, features a very different airfoil profile from that of the Clark-Y duct analyzed by Fletcher. Note the change in profile, as well as the angle of the chordline relative to the duct axis

To adequately predict the center of pressure, an angle of attack sweep from zero to thirty degrees was conducted in the SolidWorks Flow Simulation 2011 computational fluid dynamics (CFD) package. The sweep was first run for a model of a Clark-Y duct with an aspect ratio of three, with conditions matching those presented by Fletcher. These results were then compared to the experimental results presented by Fletcher to ensure the simulations provided reasonable estimates. Finally, the simulations were run for the Bluefin-21 duct (without stator) for conditions approximating those seen in the field, and error margins derived from the Clark-Y simulations were applied. For first order actuator calculations, mesh settings were kept coarse. An overview of the flow settings used is given in Table 4.1.1.

Table 4.1.1: Flow settings used for each statorless duct

	Fletcher Clark-Y	CFD Clark-Y	CFD Bluefin-21
Fluid	Air	Air	Water
Mach Number/Velocity	.13	.13	3 m/s
Static Pressure	--	101325 Pa	101325 Pa
Static Temperature	--	293.2 K	293.2 K
Dynamic Pressure	1190 Pa	1190 ± 5 Pa	4446 ± 10 Pa
Wall Roughness	--	50 μm	10 μm
Turbulence Intensity	--	10%	2 %
Turbulence Length	--	.542 mm	.542 mm
Origin (as % of chord)	25%	25%	18.9%

The results for the CFD Clark-Y duct are plotted against the results presented by Fletcher in Figure 4.1.2. The results are normalized according to Equations 4-6, where d is duct inner diameter, c is duct chord, q is dynamic pressure, L is the lifting force, D is the drag force, M is the moment about the origin, C_d is coefficient of drag, C_l is coefficient of lift, and C_m is moment coefficient. Note that the conventions are those defined in Figure 3.1.1, except moment is given the opposite sign for consistency with conventions used in the CFD results.

$$C_l = \frac{L}{qdc} \tag{4}$$

$$C_d = \frac{D}{qdc} \tag{5}$$

$$C_m = \frac{M}{qdc^2} \tag{6}$$

Results for lift, drag, and moment coefficients are in poor agreement with those presented by Fletcher: however, this is purely a function of mesh settings, and improved results are presented in Section 4.2.

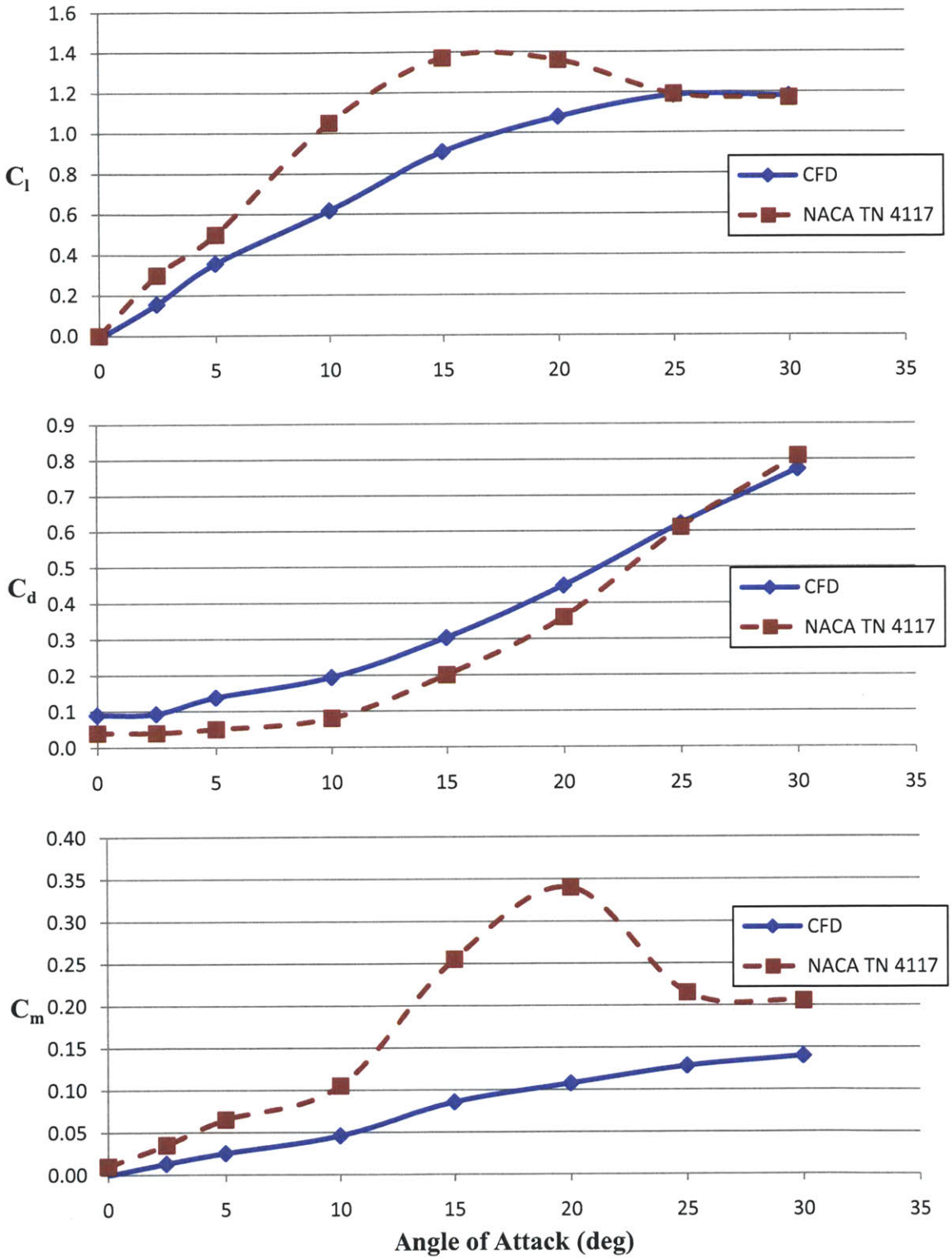

Figure 4.1.2: CFD versus experimental results for the Clark-Y duct. Agreement is poor due to coarse mesh settings.

The center of pressure for a given angle of attack is derived from lift, drag, and moment. If lift and drag are taken to act through a point along the axis of the duct, as shown in Figure 4.1.3, then their location is the point which generates the correct moment about the origin. Trigonometry and moment balance lead to Equation 7a and Equation 7b for the center of pressure as a fraction of chord length.

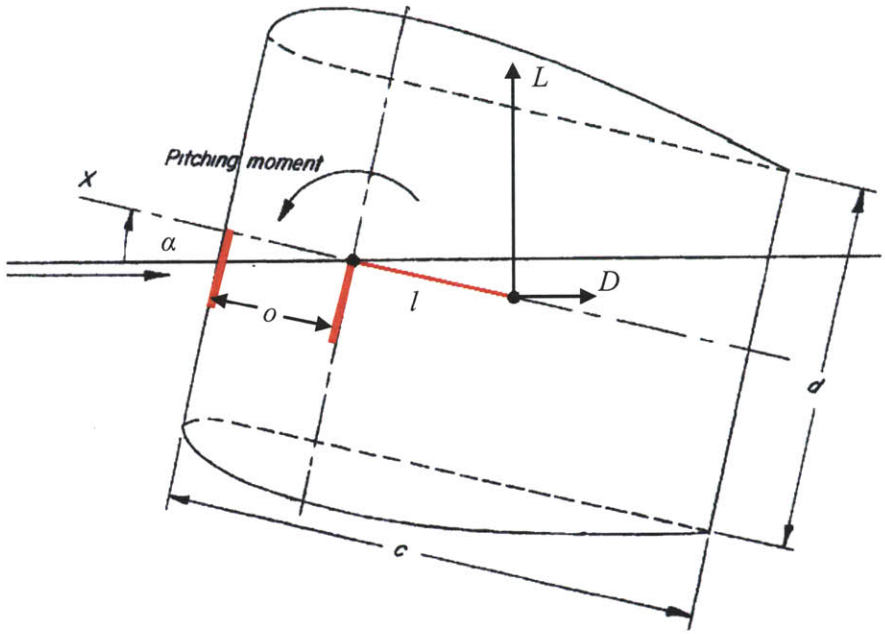

Figure 4.1.3: Lift and drag acting at the center of pressure, some distance *l* from the origin, generating a pitching moment. Image modified from Fletcher **(9)**

$$M = D \cdot l \cdot \sin(\alpha) + L \cdot l \cdot \cos(\alpha) \tag{7a}$$

$$C_m = (C_d \cdot \sin(\alpha) + C_l \cdot \cos(\alpha))\frac{l}{c}$$

$$x_{cp} = \frac{o}{c} + \frac{l}{c}$$

$$x_{cp} = \frac{o}{c} + \frac{C_m}{C_d \cdot \sin(\alpha) + C_l \cdot \cos(\alpha)} \tag{7b}$$

The center of pressure for the Clark-Y CFD results is plotted against those presented by Fletcher in Figure 4.1.4, along with the error between the two. The error in center of pressure is given by Equation 8. It is worth noting that the 22% error in center of pressure at fifteen degrees corresponds to 9.5% of chord, which is more acceptable for a first order calculation than a 22% error may be perceived.

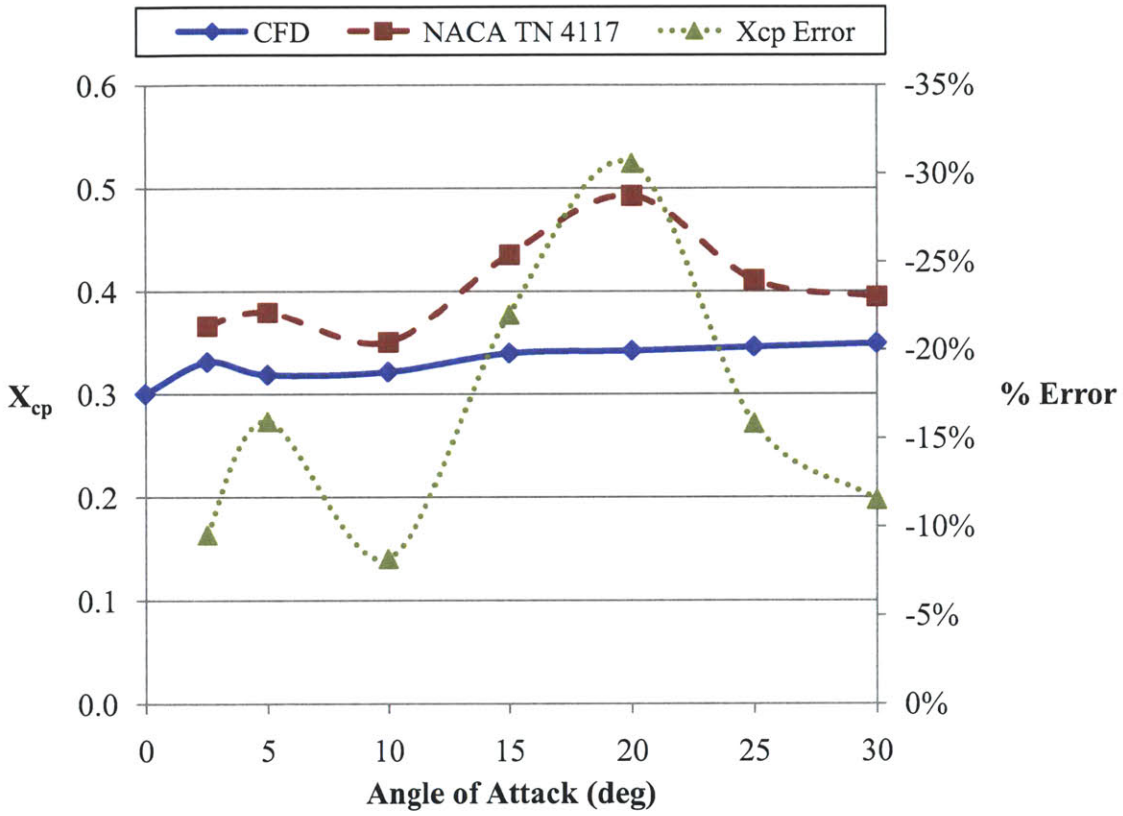

Figure 4.1.4: Experimental Clark-Y duct center of pressure results versus CFD center of pressure results. Error is given with respect to normalized center of pressure, not chord.

Using the results from CFD analysis of the Clark-Y duct, a reasonable adjustment to the CFD results for the Bluefin-21 duct can be made. The CFD results for the Bluefin-21 duct, as well as maximum estimated values computed to yield the same errors seen on the Clark-Y are shown in Figure 4.1.5.

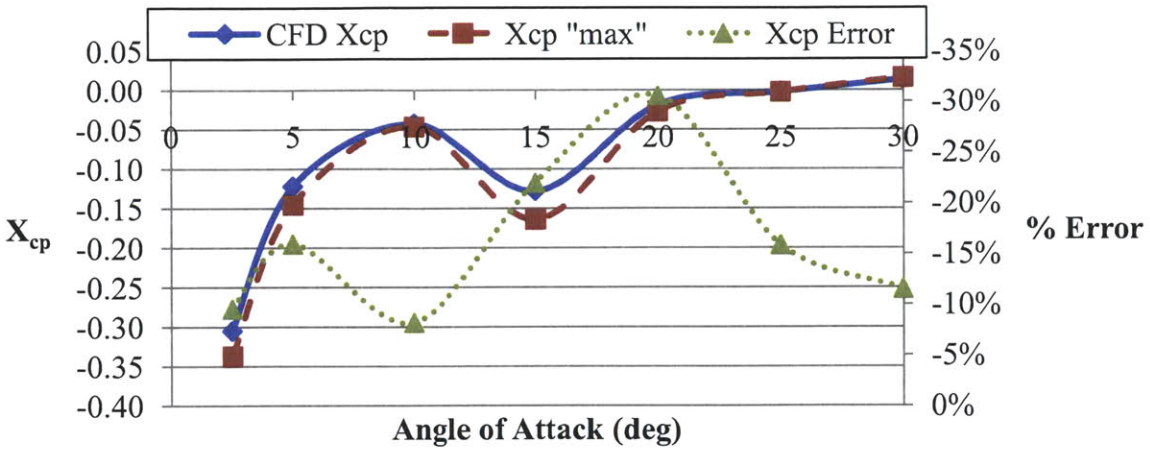

Figure 4.1.5: Center of pressure versus angle of attack for the Bluefin-21 duct. CFD results are presented, and then corrected to a maximum estimated value based on error calculations from the Clark-Y duct results.

Based on these results, the location of the center of pressure appears to in front of the leading edge of the Bluefin-21 duct. While this is beneficial in the simplification of the design (i.e. moving to a direct pivot design), a calculation error prevented this from being apparent. The moment coefficient (used in Equation 7b to find the center of pressure) was improperly calculated when the chord length c was not squared in Equation 6. This resulted in a center of pressure similar in behavior to that shown in Fletcher, so the mistake was not immediately noticed. As such, the spherical floating pivot concept was designed for less favorably placed center of pressure. As such, all remaining calculations are done with the corrected center of pressure values, but with the "incorrect" design.

In the current configuration, the pivot point and the center of pressure in the corrected (i.e. "max") fifteen degree case are 33.6 mm apart. For estimation purposes, the lift and drag properties from Fletcher are used along with a dynamic pressure of 4446 Pascals. From Equations 4, 5, and 7a, the torque about the pivot is found to be 9.9 N-m.

To account for the stator segments, it is assumed each pair acts as an elliptic wing. It can be shown that an elliptic flat plate is characterized by Equations 8-10, where A is the wing aspect ratio, D is the span, S is the planform area, and α is the angle of attack in radians. (9) (10).

$$A = \frac{D^2}{S} \tag{8}$$

$$C_l = \frac{2\pi A \cdot \alpha}{A+2} \tag{9}$$

$$C_{d,induced} = \frac{C_l^{\,2}}{\pi A} \tag{10}$$

The planform area for a pair of stator segments (herein referred to as *S*) is .01548 m^2 and the span is taken to be the diameter of the duct, resulting in an aspect ratio of 9.6. For pure yaw or pure pitch of the tailcone assembly, one stator pair is at zero angle of attack, while another pair is at the yaw/pitch angle. The two remaining pairs each see a reduced angle of attack and mutually cancel portions of their lift contributions. A geometric argument for lift cancellation is given in Figure 4.1.6.

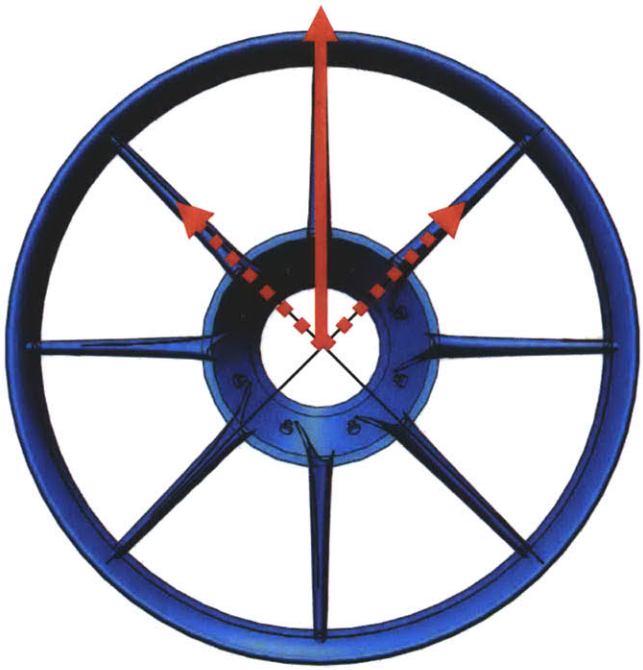

Figure 4.1.6: The horizontal lift components of the diagonal stator pairs cancel to give a purely vertical lift force.

By geometry, the angle of attack on the diagonal stator segments, α_{eff}, is given by Equation 11. Ignoring effects created by the close proximity of the segments (i.e. downwash) skin friction, walls, sweep, and details of the stator airfoil profile, the total lift and drag generated is given by Equations 12 and 13.

$$\alpha_{eff} = \tan^{-1}\left(\frac{\tan(\alpha)}{\sqrt{2}}\right) \tag{11}$$

$$L = \frac{2\pi A}{A+2}\left(\alpha + \frac{2}{\sqrt{2}} \cdot \tan^{-1}\left(\frac{\tan(\alpha)}{\sqrt{2}}\right)\right) \cdot qS \tag{12}$$

$$D = \frac{4\pi A}{(A+2)^2}\left(\alpha^2 + 2 \cdot \left[\tan^{-1}\left(\frac{\tan(\alpha)}{\sqrt{2}}\right)\right]^2\right) \cdot qS \tag{13}$$

For the area and span stated above, and using the same dynamic pressure as before, Equations 12 and 13 give the stator lift and induced drag to be 188.5 N and 8.54 N, respectively. If these forces act at same center of pressure as the duct, the torque generated by the stator segments equals 6.1 N-m. As the majority of the stator lies aft of the duct center of pressure, this is likely an overestimate. While the center of pressure of the stator segments cannot be determined accurately without some analysis of the specific geometry, it is reasonable to assume that it lies aft of the stator leading edge. Thus the stator segments may move the overall center of pressure closer to the pivot point. However, it will be assumed that they act through the same center of pressure to remain conservative in analyzing the spherical floating pivot design.

In addition to hydrodynamic loading from axial flow, some torque is required for sweeping the duct through the water, even while the vehicle is stationary. To estimate this torque, the duct is said to be moving through the water radially (i.e. angle of attack of ninety degrees). Fletcher gives the lift and drag coefficients to be 0.05 and 0.75, respectively. As such, the contribution from lift will be ignored. The density of seawater is taken to be 1025 kg/m3. The radial velocity of the duct is estimated as the product of the distance from pivot to duct center of pressure (shown to be similar at small and large angles of attack by Fletcher) and the maximum angular velocity of the duct in radians per second. Taking distance to be 33.6 mm and angular velocity to be 0.52 rad/s (as per Table 2.1.1), the radial velocity is approximately 17.6 mm/s. This velocity is two orders of magnitude smaller than the axial flow, meaning the dynamic pressure and drag will be four orders of magnitude smaller. Consequently, the torque from turning the duct in the fluid is ignored.

Finally, the gyroscopic effects of turning a spinning propeller are estimated. The propeller's moment of inertia about the shaft, as calculated in SolidWorks, is 2.4 x 10-3 kg-m2. Angular momentum, the product of inertia and angular velocity, is 0.151 kg-m2-s-1 at the

maximum propeller speed of 62.8 rad/s (3 m/s vehicle speed). Torque, the time-derivative of angular momentum, is the product of the propeller's angular momentum and the angular velocity about the pivot (0.52 rad/s from before). This results in a torque of 0.078 N-m, which is insubstantial when compared to hydrodynamic loading.

The results of the above estimates are summarized in Table 4.1.2.

Table 4.1.2: Summary of torque estimates for maximum travel in one degree of freedom (yaw or pitch) at full speed and full actuation rate.

Duct at 15 deg.	9.9 Nm
Stator at 15 deg.	6.1 Nm
Duct sweeping torque at 30 deg/s	5.7 mNm
Propeller gyroscopic torque at 30 deg/s	78 mNm
Total	**16.1 Nm**

Based on these estimates, it is possible to specify the actuators required for the spherical floating pivot design. Given the tight space constraints, it is critical that the actuator be both sufficiently powerful and compact. Since an infinitesimally small electric motor could provide infinite power were it not thermally limited, the guiding design criterion will be winding temperature. The motors considered were Faulhaber brushless DC-servomotors coupled to Faulhaber precision planetary gearheads. These were the only options considered, due to their wide selection, thorough technical data, high torque capability, and proven success in other Bluefin tailcones.

Due to the arrangement of the yaw and pitch-gear assemblies in the proposed design, the yaw actuator is used as the limiting case: the yaw gear has a smaller radius than the pitch gear, thus the highest possible reduction is smaller and the radial and tangential forces on the motor shaft are higher. Since motor torque is proportional to current, and heat generation quadratic with current, it is favorable to minimize motor torque. This can be achieved by using a large reduction ratio; however, this increases the size of the system and reduces efficiency. As such, it is favorable to maximize the reduction in the final stage (i.e. planetary gearhead to yaw-gear reduction). To begin, a yaw-gear pitch of thirty-two teeth/inch of diameter was chosen. A coarse pitch is desired for increased tooth strength while a fine pitch is desired for maximizing the final reduction. A pinion with nine teeth (the smallest number commonly available) with a pitch of thirty-two is just large enough to fit on the 2-4 mm shafts available on the smaller Faulhaber

planetary gearheads. Thus, this is taken as the limiting case, and (based on the internal dimensions of the duct) a final reduction of 20:1 is the maximum achievable. The selection of the motor is then done by the process given below.

1. Select final reduction, gearbox, and motor. Motor shaft speed (ω_{motor}) is given by Equation 14, where N_{final} is the final reduction ratio, $N_{gearbox}$ is the gearbox reduction, and ω is the required angular velocity at the duct pivot, in RPM.

$$\omega_{motor} = N_{final} \cdot N_{gearbox} \cdot \omega \tag{14}$$

2. Using the motor shaft speed, find the frictional motor torque based on frictional coefficients given in the motor spec-sheet. The frictional motor torque τ_f is given by Equation 15, where C_o is the static friction torque and C_v is the dynamic friction torque.

$$\tau_f = C_o + C_v \cdot \omega_{motor} \tag{15}$$

3. The total torque demanded of the motor (τ_{motor}) should be calculated. This can be found by Equation 16, where $\eta_{gearbox}$ is the efficiency of the planetary gearhead, η_{final} is the efficiency of the final reduction, and τ_{pivot} is the torque about the duct pivot.

$$\tau_{motor} = \tau_f + \frac{\tau_{pivot}}{N_{final} \cdot N_{gearbox} \cdot \eta_{final} \cdot \eta_{gearbox}} \tag{16}$$

4. The power dissipated by the windings (P_w) is then found by Equation 17, in which R is the winding resistance and K_m is the torque constant of the motor.

$$P_w = \left(\frac{\tau_{motor}}{K_t} \right)^2 \cdot R \tag{17}$$

5. Based on this power dissipation, the maximum allowable housing-to-ambient thermal resistance ($R_{th,2}$) can be found by Equation 18. T_{max} is the maximum allowable winding temperature, T_a is the ambient temperature, and $R_{th,1}$ is the thermal resistance between the windings and the housing.

$$R_{th,2} = \frac{T_{\max} - T_a}{P_w} - R_{th,1} \tag{18}$$

6. The maximum allowable housing-to-ambient thermal resistance should be compared to the nominal value provided by Faulhaber. Reductions in thermal resistance are achievable

through heat-sinking and other thermal management techniques, but large reductions in thermal resistance are difficult to achieve.

7. Voltages, speeds, and loads should be checked using basic motor constitutive relationships to ensure operation is within reasonable limits. Repeat the process until a suitable actuator/gearbox combination is selected.

Table 4.1.3 presents a sample actuator selection. The actuator selected here is the six volt Faulhaber 1226-006-B brushless DC-servomotor coupled to the Faulhaber 256:1 12/4K planetary gearhead, whose spec-sheets are given in references (11) and (12). This motor and gearbox combination is used in the solid models presented in Figures 3.2.5.1 through 3.2.5.5. It will continue to be the actuator selection for the remainder of the design study.

Table 4.1.3: A sample actuator and gearbox selection process is shown. In this case, the housing-to-ambient thermal resistance must be 10% of nominal to avoid damaging the motor. It is important to note that this is achievable, and that the torque estimates are incredibly conservative.

Motor	Faulhaber 1226	*6 V windings*		
Gearhead	Faulhaber 12/4			
Final Drive Ratio	20.000			
Gearhead Ratio	256			
Gearhead Efficiency	60%			
Max RPM @ Pivot	5			
Max Torque @ Pivot(Nm)	16.1		*Cont.*	*Int.*
Max Torque @ Gearhead (Nm)	0.847	**Rated**	0.3	0.45
Torque @ Motor (Nm)	0.0052	**Stall**	7.19	*mNm*
Motor RPM	25600	**Max**	60000	--
Dynamic+Static Friction (Nm)	0.00028892			
Speed Constant	3447	*rpm/V*		
Torque Constant	2.77	*mNm/A*		
Resistance	2.3	*Ω*		
Back EMF	7.426747897	*V*		
Current	2.096	*A*		
Voltage Drop	4.82	*V*		
Coulomb Loss	10.1	*W*		
Max Operating Temp	125	*C*		
Ambient	22	*C*		
Coil-Housing Resistance	7	*K/W*		
Housing Air Resistance (nom)	38	*K/W*		
Max act. Housing-Air Resist.	3.195	*K/W*		
Percent Reduction	92%			

4.2. Additional Hydrodynamic Analysis

While the models presented in Section 4.1 are adequate for initial feasibility assessment, more accurate models are desirable when pursuing a detailed design analysis, as is done in Sections 4.3 and 4.4. To improve the accuracy of load-related estimates, these three additions were made:

- Improved characterization of duct hydrodynamics
- Modeling of propeller thrust
- Torque about duct axis

To improve hydrodynamics characterization, the mesh and convergence settings in SolidWorks Flow Simulation 2011 were adjusted. To verify that the new settings gave more realistic results, they were first tested on the Clark-Y duct used in Fletcher's experiments and compared with his results. The same settings were then applied to the Bluefin-21 duct. The resulting center of pressure is presented in Figure 4.2.1. All sets of lift, drag, and moment data are plotted in Figure 4.2.2 (based on the conventions and general settings used in Section 4.1). The agreement between experimental and CFD results is much improved, and it is now reasonable to use the corrected Bluefin-21 CFD results for calculation of duct forces and moments. As before, the Bluefin-21 values are corrected using the error between the Clark-Y experimental and CFD results.

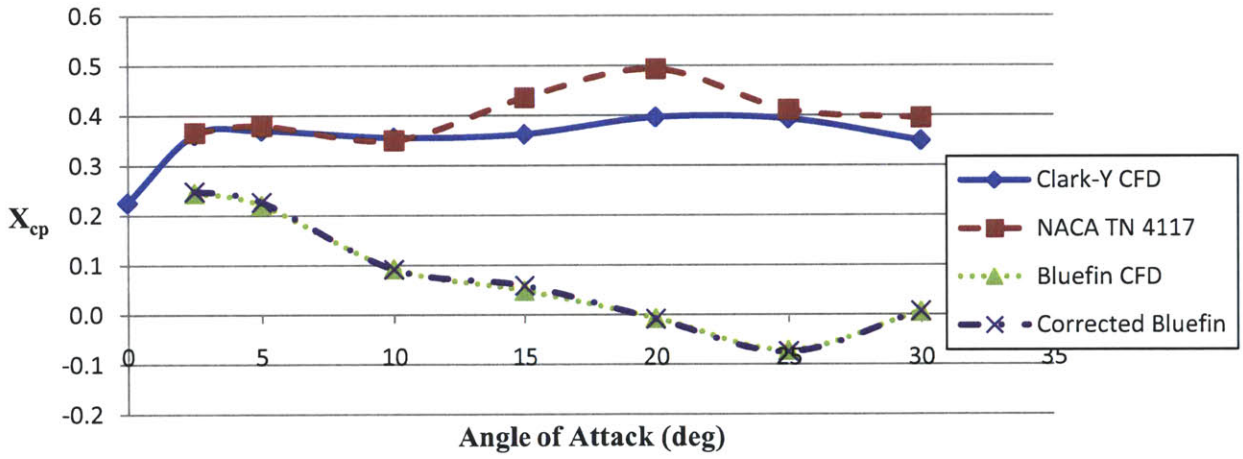

Figure 4.2.1: The center of pressure versus angle of attack for both Clark-Y and Bluefin Duct. The agreement between the Clark-Y CFD and experimental is much improved.

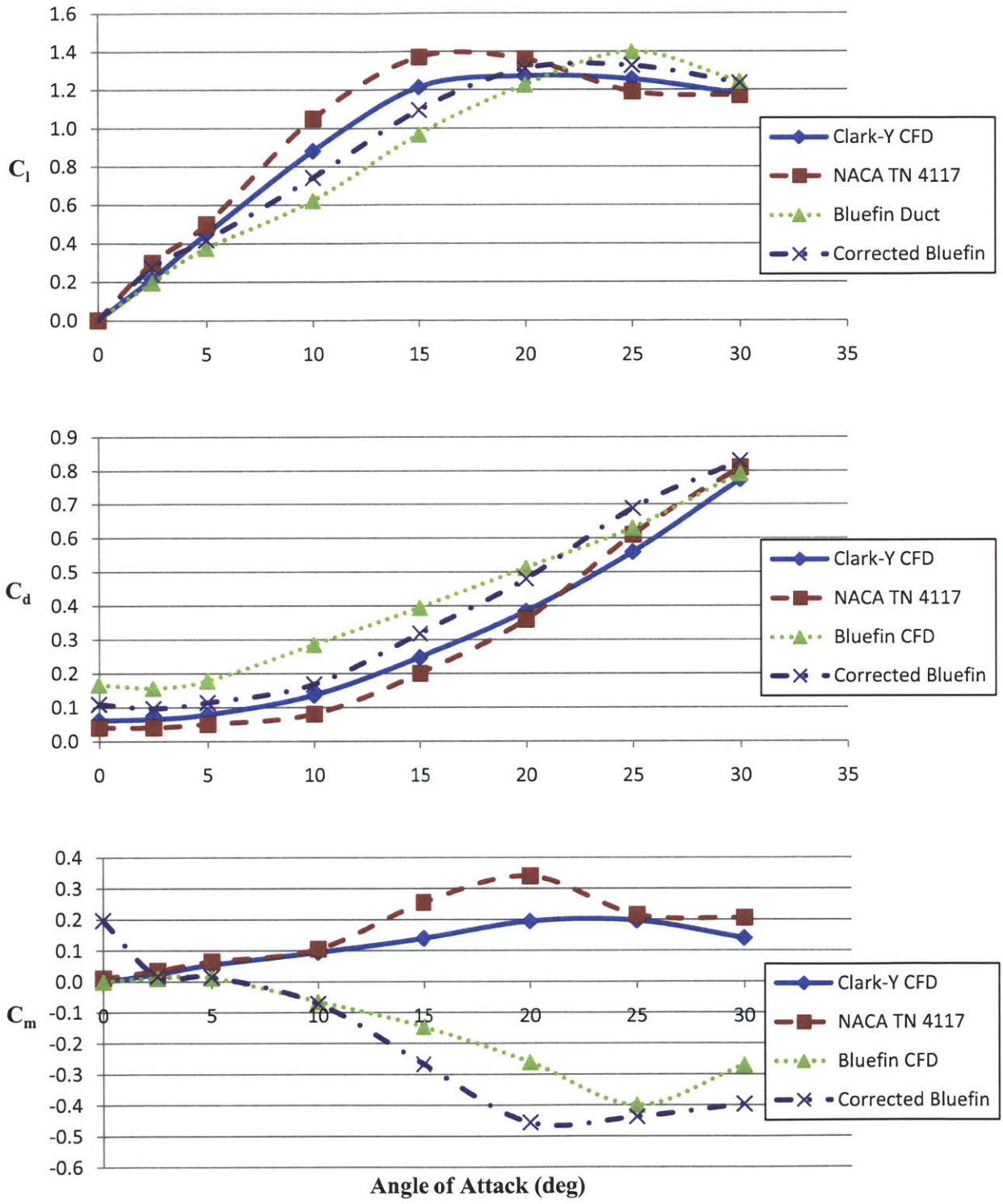

Figure 4.2.2: Plots of lift, drag, and moment coefficients for both Clark-Y and Bluefin-21 ducts. The agreement between Clark-Y CFD results and Fletcher's experimental results is improved over those presented in Section 4.1.

In addition to duct lift and drag forces, the tailcone experiences a thrust load from the propeller. Propeller torque and angular velocity calculations were provided by Bluefin and are presented in Table 4.2.1. A constant propulsor efficiency of 65% is assumed, meaning 65% of shaft power goes into propulsive power (the product of propulsive for and vehicle speed). From this, propeller force is easily found. It is assumed that propeller force is always axial along the duct. A plot of the axial force is shown in Figure 4.2.3, along with a quadratic equation for calculating force as a function of vehicle speed.

Table 4.2.1: Propeller angular velocity, torque, power, and axial force as a function of vehicle speed.

Speed *m/s*	**Prop Speed** *rad/s*	**Prop Torque** *Nm*	**Prop Power** *W*	**Jet Force** *N*
0	0.0	0	0	0
1.0288	20.9	3	63	40
1.5432	31.4	6.5	204	86
2.0576	41.9	11.2	469	148
2.572	52.4	17.2	900	228
3.0864	62.8	24.5	1539	324

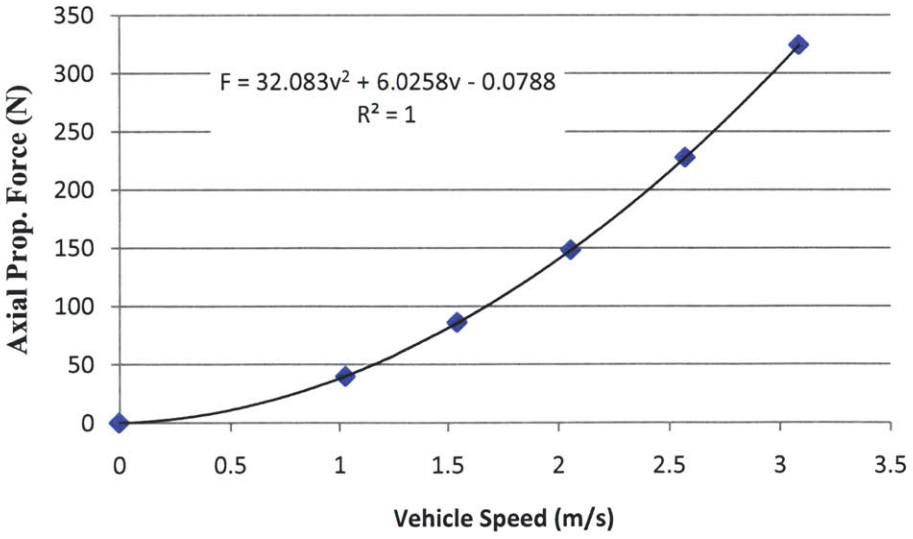

Figure 4.2.3: Propeller axial force as a function of vehicle speed. Note that the force is exactly quadratic with vehicle speed.

Due to the drag torque associated with the propeller, the stator of the duct must provide an opposing torque. A reasonable estimate for this opposing moment suggests that the torque provided be exactly equal to the propeller shaft torque. It is assumed that the axial moment created by the duct always be directed to the front of the vehicle, along the duct axis. If the duct axis is not aligned with the freestream flow, then the moment is not aligned with the freestream: it remains aligned with the duct axis, and equal in magnitude to the propeller shaft torque.

4.3. Load Analysis and Bearing Selection

With a more complete model for loads imposed on the tailcone, a number of components can now be analyzed. Five categories of components were analyzed in this study:

- Shaft and propeller bearings
- Gear teeth
- Motor shafts
- Ball transfers
- Floating gear support bearings

The shaft, propeller, and floating gear bearings are all governed by the same models. A bearing cannot exceed its rated static load (else it will yield), and its lifetime is estimated by the rated dynamic load. A combination of radial and thrust loads on a bearing can be equated to an equivalent radial load for life calculations. Beyond lifetime and yield criteria, all bearings are subject to strong dimensional constraints in the spherical floating pivot design. The floating gear support bearings must fit within the yaw-gear assembly, which is constrained by the spherical housing; the shaft bearings must be enclosed within the primary support beam, which has a highly constrained diameter because of the spherical housing; the propeller bearings must fit within the duct (i.e. sufficiently small outer diameter) while providing adequate clearance for the propeller shaft (sufficiently large inner diameter). As such, the selection of bearings is a highly iterative process, and the bearings specified in this study are simply used to demonstrate feasibility.

In this study, bearings are assumed to come from The Timken Company, and lifetimes are therefore evaluated by the Timken specifications. The lifetime of a bearing is given by Equation 19, where lifetime L_H is the number of hours of operation that 90% of a group of

identical bearings will endure, C is the dynamic load rating, R is the equivalent pure radial load, and N is the angular velocity of the inner race, in RPM (13).

$$L_H = \frac{16667}{N}\left(\frac{C}{R}\right)^3 \tag{19}$$

The equivalent radial load (R) can be found using Equation 20 and Table 4.3.1, where F_a is the axial load, F_r is the radial load, and C_o is the basic static load rating of the bearing (14).

$$R = X_i \cdot F_r + Y_i \cdot F_a \tag{20}$$

Table 4.3.1: Equivalent radial load factors for ball bearings, adapted from *Shigley's Mechanical Engineering Design* **(14)**

		$F_a/F_r \leq e$		$F_a/F_r \geq e$	
F_a/C_o	e	X_1	Y_1	X_2	Y_2
0.014	0.19	1.00	0	0.56	2.30
0.021	0.21	1.00	0	0.56	2.15
0.028	0.22	1.00	0	0.56	1.99
0.042	0.24	1.00	0	0.56	1.85
0.056	0.26	1.00	0	0.56	1.71
0.070	0.27	1.00	0	0.56	1.63
0.084	0.28	1.00	0	0.56	1.55
0.110	0.30	1.00	0	0.56	1.45
0.17	0.34	1.00	0	0.56	1.31
0.28	0.38	1.00	0	0.56	1.15
0.42	0.42	1.00	0	0.56	1.04
0.56	0.44	1.00	0	0.56	1.00

Worst-case loading of the shaft and propeller bearings occurs when only one segment of the tripod joint is transferring torque, as shown in Figure 4.3.1. In this case, the force acting at a radius to generate the requisite torque is not cancelled by symmetry, and the bearings see a radial load. For a maximum shaft torque of 25 N-m, acting at a radius of 0.8 inches, a radial force of 1230 N (277 lbs) is generated at the tripod joint. Coupled with a maximum thrust load of 324 N (see Table 4.2.1) from the propeller at 600 rpm, Equations 19-20 and Table 4.3.1 give a predicted life of 1133 hours for the Timken bearing outline in Table 4.3.2. While this is fairly

low life for a bearing, it is also assuming worst-case loading. The bearing outlined in Table 4.3.2 also proves to be reasonably sized for packaging into the duct.

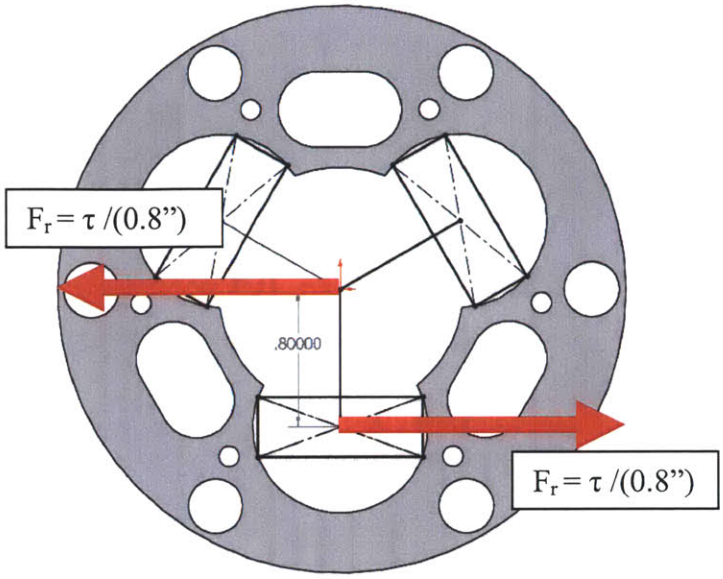

Figure 4.3.1: An axial view of a tripod joint, illustrating single-point-of-contact torque generation: the worst-case radial loading possible for tripod bearings, propeller bearings, and propeller shaft bearings.

Table 4.3.2: Basic specifications for a thin section Timken bearing for application as a propeller support bearing **(13)**

Bearing Series	Timken Thin Section Series
Bearing Type	Conrad Assembly
Basic Bearing Size	3240
Bore	2"
O.D.	2.5"
Width	0.25"
Dynamic Radial Load (C)	952 lbs
Static Radial Load (C_0)	1016 lbs
Static Thrust Load	1003 lbs

The same worst-case radial loading is seen by the propeller shaft. The shaft is also cantilevered from the end of the primary support beam to the tripod joint; the tripod joint is 186 mm from the base of the propeller shaft, and the bearing is 136 mm from the base. As a result, the propeller shaft bearing experiences 1.38 times the radial force seen at the tripod joint (1682 N). The bearing outlined in Table 4.3.3 (and shown in the solid models of the spherical floating

pivot design) would only last 160 hours under this loading condition; however, this is again worst-case.

Table 4.3.3: Basic specifications for a torque tube Timken bearing for application as a propeller shaft bearing **(13)**

Bearing Series	Timken Torque Tube Series
Bearing Type	Conrad Assembly
Basic Bearing Size	1421
Bore	.875"
O.D.	1.3125"
Width	0.250"
Dynamic Radial Load (C)	679 lbs
Static Radial Load (C_o)	433 lbs
Static Thrust Load	481 lbs

To assess the remaining components, a detailed statics model must be developed. To begin, a coordinate system is defined. This is done so in Figure 4.3.2. The x-axis is defined as axial to the vehicle, positive in the aft direction. The z-axis is positive upwards, and the y-axis is defined to create a right-hand coordinate system. The origin is at the pivot point of the duct.

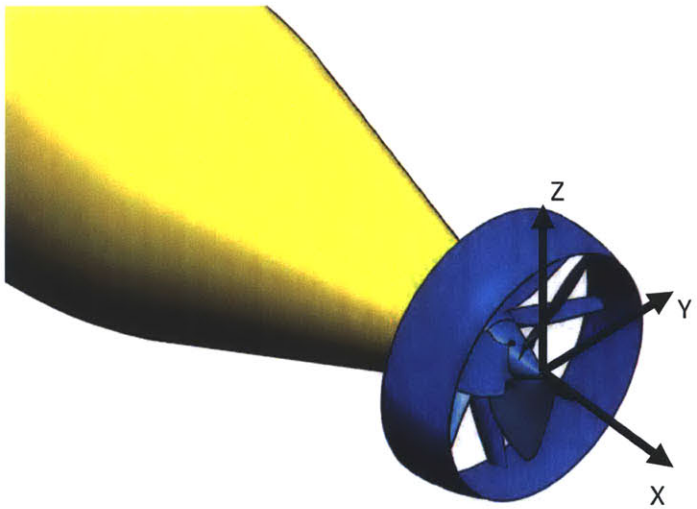

Figure 4.3.2: Coordinate system used for developing statics model.

The statics model is simply a solution of force and moment balance. Since the origin is taken at the pivot point, and the ball transfers generate a force directly through the origin, it is simplest to begin with moment balance about the origin. There are four factors that contribute to moment about the origin:

- Moment generated from lift and drag at the center of pressure
- Moment generated by the drag-torque cancelling stator
- Moment generated by the pitch motor
- Moment generated by the yaw motor

To simplify finding moments generated by the duct and stator, it is useful to define an effective angle of attack (α) and a lift angle (β) in terms of yaw angle (φ) and pitch angle (θ). These terms are defined in Figure 4.3.3 and Equations 21 and 22.

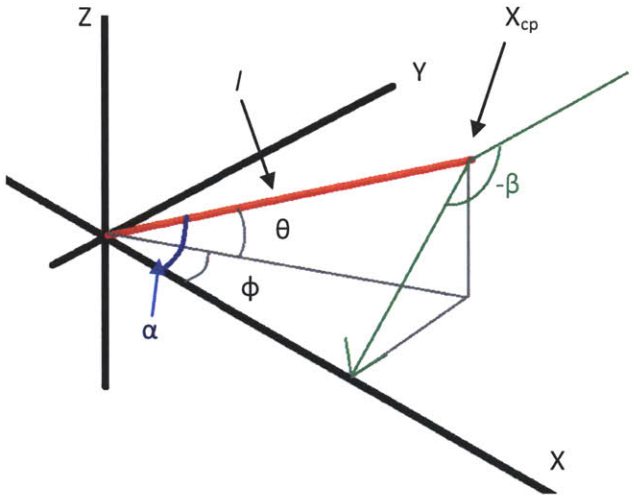

Figure 4.3.3: Definition of effective angle of attack and lift angle, with respect to vehicle coordinate system.

$$\tan(\alpha) = \sqrt{\frac{\sin^2(\phi) + \tan^2(\theta)}{\cos^2(\phi)}} \tag{21}$$

$$\tan(\beta) = \frac{\tan(\theta)}{\sin(\phi)} \tag{22}$$

With these definitions, the moments generated by the duct and stator are easily derived. Recalling that the stator generates a moment (equal to propeller torque) directed from the center

of pressure to the origin, lift acts along the lift angle, and drag acts along the x-axis, the moments generated by the duct and stator are given by Equations 23 through 25.

$$M_{x,duct} = -\tau_{stator} \cdot \cos(\alpha) \tag{23}$$

$$M_{y,duct} = \tau_{stator} \cdot \sin(\alpha) \cdot \cos(\beta) - L \cdot l \cdot \cos(\alpha) \cdot \sin(\beta) + D \cdot l \cdot \sin(\alpha) \cdot \sin(\beta) \tag{24}$$

$$M_{z,duct} = \tau_{stator} \cdot \sin(\alpha) \cdot \sin(\beta) + L \cdot l \cdot \cos(\alpha) \cdot \cos(\beta) + D \cdot l \cdot \sin(\alpha) \cdot \cos(\beta) \tag{25}$$

The distance between the origin and the center of pressure is given by l; the lift L is found by combining the results of Equation 12 with the CFD results presented in Section 4.1; the drag D is found by combining Equation 13 with CFD results from Section 4.1; and τ_{stator} is found by quadratic interpolation of propeller torque from Table 4.2.1.

Next, the contribution of the yaw actuator to moment balance is accounted for. Figure 4.3.4 defines the placement of the yaw motor. The pitch radius of the yaw-gear assembly is r_{yaw}; the height of the yaw pinion above the x-y plane is defined as z; the angle at which the yaw-pinion engages relative to the x-axis is given as θ_1; the tangential force at the gear-pinion interface is F_{t1}; the radial force at the gear-pinion interface is F_{r1}; and the gear pressure angle is defined as θ_{pa}. Figure 4.3.5 defines the analogous terms for the pitch motor; however, this is given in the x`y`z` coordinate system, which is rotated about the z-axis by yaw-angle φ (a result of the pitch actuator being mounted on the yaw-gear assembly).

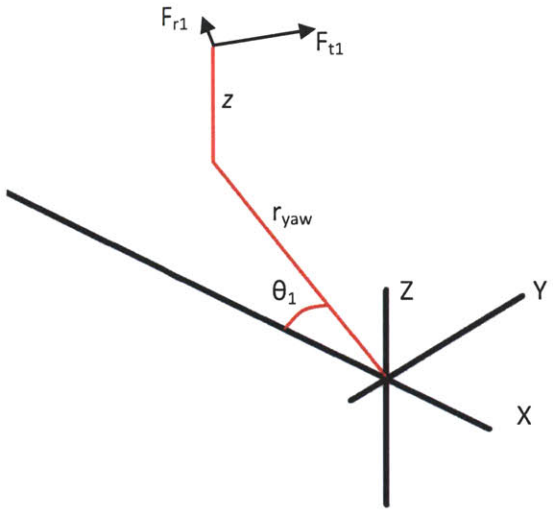

Figure 4.3.4: Yaw-gear/yaw-pinion geometry definitions for use in static force and moment balance.

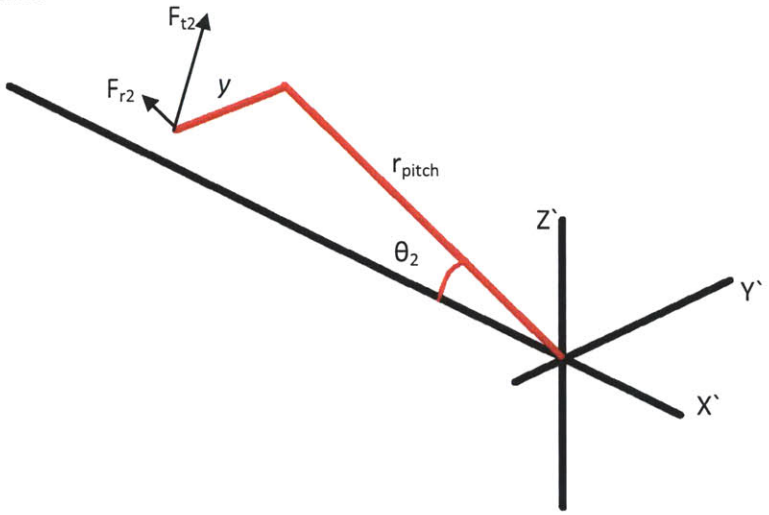

Figure 4.3.5: Pitch-gear/pitch-pinion geometry definitions for use in static force and moment balance.

The moment contributions from the yaw and pitch gears are given by Equations 26 through 34.

$$F_{ri} = \left| F_{ti} \cdot \tan(\theta_{pa}) \right| \tag{26}$$

$$M_{x1} = -F_{t1} \cdot z \cdot \cos(\theta_1) - F_{r1} \cdot z \cdot \sin(\theta_1) \tag{27}$$

$$M_{y1} = F_{t1} \cdot z \cdot \sin(\theta_1) - F_{r1} \cdot z \cdot \cos(\theta_1) \tag{28}$$

$$M_{z1} = -F_{t1} \cdot r_{yaw} \tag{29}$$

$$M`_{x2} = -F_{t2} \cdot y \cdot \cos(\theta_2) - F_{r2} \cdot y \cdot \sin(\theta_2) \quad (30)$$

$$M_{z2} = F_{t2} \cdot y \cdot \sin(\theta_2) - F_{r2} \cdot y \cdot \cos(\theta_2) \quad (31)$$

$$M`_{y2} = F_{t2} \cdot r_{pitch} \quad (32)$$

$$M_{x2} = M`_{x2} \cdot \cos(\phi) - M`_{y2} \cdot \sin(\phi) \quad (33)$$

$$M_{y2} = M`_{x2} \cdot \sin(\phi) + M`_{y2} \cdot \cos(\phi) \quad (34)$$

Since there are only two unknowns in this system (yaw and pitch motor tangential forces), moment balance around the z-axis and the y-axis is sufficient to solve for these forces. The sum of moments about the x-axis is then used to find the forces required of the floating gear support bearings. Using these results, the sum of forces (excluding ball transfers) can be found. Net force is set to zero and the force balance is used to solve for the ball transfer reaction forces. Force balance provides three equations (x-force, y-force, and z-force); there are four ball transfers, thus four unknowns. However, ball transfers can only apply a positive radial force, so one reaction force can always be set to zero. The solution may require some iteration to ensure that no ball transfer reaction force is negative.

A summary of the geometry used is given in Table 4.3.4, and a summary of the maximum forces experienced by various components is given in Table 4.3.5. In this case, support 1 is treated as the starboard-side inner support, support 4 is the port-side inner support, support 3 is the lower outer support, and support 2 is the upper outer support. The support angle is the defined as the angle between the reaction forces of the relevant supports.

Table 4.3.4: Summary of the geometry used in solution of component forces.

Pivot Geometry		
Leading edge to pivot	0.525"	0.0133 m
Inner Spherical Housing Radius	3.937"	0.1000 m
Outer Spherical Housing Radius	3.937"	0.1000 m
Yaw Gearing Geometry		
Yaw gear radius	2.813"	0.0714 m
Yaw pinion radius	0.141"	0.0036 m
Angle from centerline	16.26°	0.284 rad
Yaw gear Z offset	1.134"	0.0288 m
Pressure angle	20.0°	0.349 rad
Pitch Gearing Geometry		
Pitch gear radius	2.813"	0.0714 m
Pitch pinion radius	0.141"	0.0036 m
Angle from centerline	16.26°	0.284 rad
Pitch gear Y offset	1.134"	0.0288 m
Pressure angle	20.0°	0.349 rad
Support Geometry		
Inner Support Angle	65.8°	1.148 rad
Outer Support Angle	65.8°	1.148 rad
Ball Transfer Diameter	0.500"	0.013 m

Table 4.3.5: Summary of maximum forces experienced by various components over +/- ten degree travel in pitch and yaw.

Max Yaw Actuator Torque	0.321 Nm
Max Yaw Actuator Radial Force	95.489 N
Max Pitch Actuator Torque	0.377 Nm
Max Pitch Actuator Radial Force	112.432 N
Max Torque about X axis	26.832 Nm
Max Load on Support 1	723.043 N
Max Load on Support 2	695.827 N
Max Load on Support 3	808.729 N
Max Load on Support 4	728.701 N

Based on the radial forces required at the actuators, a maximum tooth load is known for the gears and pinions of the pitch and yaw assemblies. Though the radial load at the actuator is due to both tangential and radial loads at the tooth (torque-transferring and separation forces), it

is assumed that the resultant force is purely tangential for a worst case estimate. Gear teeth can be treated as simple beams with a correction factor for tooth geometry. Under these assumptions, the Lewis Formula gives the maximum safe working load W as Equation 35, where S is one third the material tensile strength, F is the face width of the gear, Y is the Lewis Y factor tabulated for various tooth geometries, and P is the diametrical pitch (15).

$$W = \frac{S * F * Y}{P} \tag{35}$$

1040 steel with a face width of .125", a tensile strength of 90 ksi, a pitch of 32, and a 10 tooth pinion can withstand 105 Newtons of force, which is slightly less than the maximum force required for the pitch actuator. However, stronger materials area available, the face width may be increased, and the load estimates can likely be relaxed. As such, the desired gear dimensions seem feasible.

Unfortunately, the Faulhaber gearhead demands less than 20 Newtons of radial force (12), which is approximately 20% of that required in this design configuration. While this can be worked around by adding adapters to doubly support the shaft, it is more desirable to adjust the pivot point or use less conservative estimates for the hydrodynamic loading of the duct stator before introducing additional parts and bearings.

Perhaps the most critical components in the spherical floating pivot design, the ball transfers see some of the highest loads. While a brief review of the McMaster-Carr catalogue reveals a suitable option with half inch hardened steel ball (as per the current design), it has a maximum load of only 450 N; 55% of that which is demanded. However, it is feasible that not only will these loads decrease as a more refined loading model is developed; it is also very plausible that there exist stronger ball transfer units of similar dimensions. Beyond basic load ratings, however, exists another ball-transfer problem: Hertzian contact stresses. When two round surfaces contact, as in this case, they create infinitesimally small contact areas that see large contact forces. These generate large stresses beneath the surface. The contact area radius a can be found by Equation 36, where E and ν are the elastic constants of their respective materials, F is the normal force, and d is the diameter of each component (flat plate being infinite and concave surfaces being negative). The maximum pressure P is then found by Equation 37.

Using Equations 38 and 39, the principle stresses can be found (using z as the depth below the surface), and used in Equation 40 to calculate the von Mises Stress (16).

$$a = \sqrt[3]{\frac{3F}{8}\frac{(1-\nu_1)^2/E_1 + (1-\nu_2)^2/E_2}{1/d_1 + 1/d_2}} \tag{36}$$

$$P = \frac{3F}{2\pi a^2} \tag{37}$$

$$\sigma_1 = \sigma_2 = -P\left[\left(1 - \left|\frac{z}{a}\right|\tan^{-1}\frac{1}{|z/a|}\right)(1+\nu) - \frac{1}{2(1+\frac{z^2}{a^2})}\right] \tag{38}$$

$$\sigma_3 = \frac{-P}{1+\frac{z^2}{a^2}} \tag{39}$$

$$\sigma_{vonMises} = \left[\frac{(\sigma_1-\sigma_2)^2 + (\sigma_2-\sigma_3)^2 + (\sigma_3-\sigma_1)^2}{2}\right]^{1/2} \tag{40}$$

A plot of the von Mises Stress (normalized by yield stress) versus depth (normalized by contact area radius) is shown in Figure 4.3.6. Table 4.3.6 shows the material properties assumed for the spherical housing and ball transfers. From this, it is visible that the housing and ball transfers may experience yield below the surface. However, with reduced forces expected from improved pivot placement, this should not be a problem, as both are only slightly above yield. The unfortunate requirement is that the spherical housing be made of hardened steel: aluminum and titanium prove to exceed their yield strength be a factor of three or more.

Table 4.3.6: Material properties of ball transfers and spherical housing.

Ball ν	0.29		M50 Steel
Ball E	203	*GPa*	
Ball Yield	2206	*MPa*	
Housing ν	0.29		M50 Steel
Housing E	203	*GPa*	
Housing Yield	2206	*MPa*	

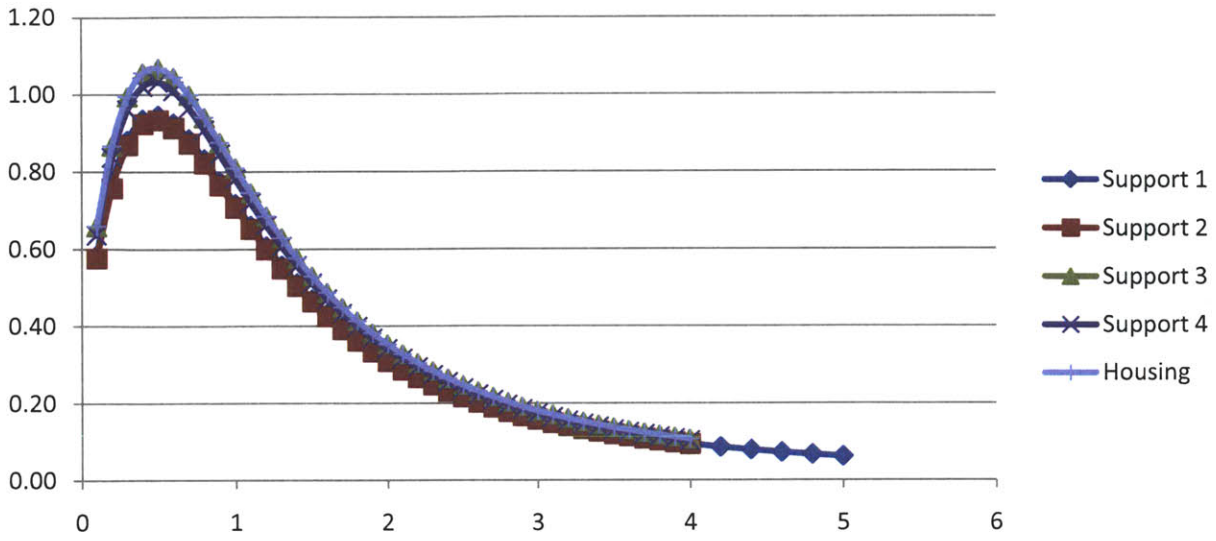

Figure 4.3.6: Hertzian contact normalized von Mises Stress versus normalize depth in the spherical housing and ball transfers.

5. DESIGN EVALUATION

5.1. Feasibility

The proposed spherical floating pivot design outlined above raises a number of feasibility concerns. The first among these is whether components can survive the forces required of them. While it seems that motor and gearbox are within limits, the thermal coupling required to adequately cool the motor under full range of motion is unnerving, but not impossible. An adequately sized actuator is certainly attainable if different gearhead/final-drive combinations are pursued. Bearings and gears do not seem to raise major concerns for this design. The biggest concern, however, is the loading seen by the ball transfers. The Hertzian contact stresses induced suggest that both the housing and some of the balls will yield. Fortunately, all loading estimates are highly conservative, and most every component is within a factor of two of its maximum load. Clever materials choice, slight geometry refinements, and pivot relocation can easily alleviate these concerns.

Another concern raised by this design is the limited pitch-yaw motion. Due to the location of the pivot, the spherical housing was only able to encompass approximately sixty

degrees angular area. This equates to +/- ten degrees in each direction. This simply does not meet requirements, but is easily averted if the pivot point is moved further forward on the vehicle. Doing so will allow the spherical housing to capture a larger angle of the desired arc, increasing range of travel. However, the diameter of the spherical surface will become smaller, affecting Hertzian contact stresses.

The spherical housing must also be made of hardened steel. The steel can be machined and hardened post-machining, but the process will likely be costly. Additionally, steel is a poor material choice for underwater operation, especially in high salinity environments. Therefore, the housing would have to receive an anti-corrosion coating, adding additional cost.

Finally, the entire system is difficult to seal. There are very few surfaces available for sealing overall, and those that exist are complex and bulky. The tripod housing seal requires a large diameter rotating seal, while the spherical housing will likely require a difficult to engineer rolling seal. However, these are all solvable issues, and result in a much more compact tailcone.

5.2. Future Modeling Work

Before further design progress can be made, additional modeling efforts must be made. Most importantly, the hydrodynamics modeling must be improved. The duct stator needs to be modeled in more detail, either with CFD or through vortex panel methods. The effects of adjacent stators should be taken into account, as well as the wall effects from the duct and the duct mounting. Ideally, the unit would be modeled as on complete unit, allowing for all fluid interactions to be accounted for. This would yield an improved center of pressure estimate, as well as improved estimates of the loads seen on all components.

Additional component stresses should be modeled: namely, the Hertzian contact between the floating-gear assembly support bearings and their associated troughs, as well as the yaw and pitch gear assemblies themselves. Both see unusual loading from the duct attempting to rotate along the x-axis of the vehicle, and this could prove to be a catastrophic weak point.

The resonance of the system should also be investigated to ensure that no components see frequencies which could excite natural modes. The primary concern is the propeller shaft, which could see vibrations from the tripod joint, and the primary support beam, which sees changing loads as the duct is repositioned.

5.3. Recommended Design Alterations

The proposed design could benefit from a number of changes. Perhaps the most critical change it the repositioning of the pivot point. Since the center of pressure proved to be further forward on the duct (in front of the leading edge), it is possible to relocate the pivot point to a less geometrically constrained area. This allows the tripod housing more room for mounting, easing bearing selection and seal design. This also decreases the radius of the spherical housing, which allows a larger angle to be swept out by its arc. This results in the desired range of motion. Replacing the tripod joint with a flexure coupling will also increase space within the duct for actuators, as well as simplify bearing and seal design.

The symmetry of the design could be better utilized by adding an additional actuator for each degree of freedom. This would simplify the floating gear loading, as more forces would cancel by symmetry. In addition, the actuators could be downsized as a result of sharing their loads. This modification would also provide increased redundancy, in case of an actuator failure.

6. CONCLUSION

In an effort to improve the payload capability of the Bluefin-21 AUV, an alternative thrust-vectoring tailcone design was desired. To achieve a more compact tailcone design, a number of design strategies were considered: alternative actuation, alternative component packaging, and pivot relocation. The pivot relocation strategy proved to be the most beneficial: mounting the pivot point at the center of pressure dramatically reduces forces and downsizes actuators and components. To accomplish this strategy, three concept strategies were pursued. The concept strategies included a traditional direct pivot design, a push-rod style design, and a floating pivot design. Of these, the floating pivot looked most favorable for its ability to minimally affect hydrodynamics and duct design. The components could be located elsewhere in the vehicle and accomplish the mandatory pivoting motion by being constrained to a specific arc. Upon deciding on this architecture, a detailed design concept was developed.

Upon development of the concept, hydrodynamic modeling (namely CFD) was utilized to predict forces on the system. From there, a statics model was developed to predict individual component forces. These forces were used to assess bearings, contact stresses, actuator loading, and other components. Based on this information, the design was able to be verified as a feasible design.

A number of design improvements are suggested, providing a stepping stone for further design development. Additional modeling suggestions are also made, allowing the design to be refined to a greater level of certainty. Overall, the design proves feasible, albeit complex. The overall volumes saving, however, are significant.

7. REFERENCES

1. **National Aeronautics and Space Administration.** Gimbaled Thrust. *NASA.gov.* [Online] [Cited: May 25th, 2012.] http://exploration.grc.nasa.gov/education/rocket/gimbaled.html.

2. **Bluefin Robotics Corporation.** Bluefin-21. *Bluefin Robotics Corporation.* [Online] 2012. [Cited: May 25, 2012.] http://www.bluefinrobotics.com/products/bluefin-21/.

3. **Aerotech Inc.** S Series Brushless, Frameless Torque Motors. *Aerotech.com.* [Online] 2012. [Cited: May 25, 2012.] http://www.aerotech.com/product-catalog/motors/rotary-motors/s-series-brushless-frameless-torque-motors.aspx?p=%2fproduct-catalog%2fmotors%2frotary-motors.aspx%3f.

4. **Nutzdatenbegleiter.** File:Gelenk-welle.jpg. *wikipedia.* [Online] July 18, 2008. [Cited: May 25, 2012.] http://en.wikipedia.org/wiki/File:Gelenk-welle.jpg.

5. **Ali, Soheel.** C.V. Joints & Driveshafts. *TTEC 4844- Transmissions and Drivelines.* [Online] June 12, 2911. [Cited: May 25, 2012.] http://soheelali.blogspot.com/2011/06/cv-joints-driveshafts.html.

6. **EngineerLive.** How to maximise the benefits of custom couplings. *EngineerLive.com.* [Online] [Cited: May 25, 2012.] http://www.engineerlive.com/Asia-Pacific-Engineer/Power_Transmission/How_to_maximise_the_benefits_of_custom_couplings/23204/.

7. **China East Mechanical Transmission.** Needle Bearing Universal Joint. *China East Mechanical Transmission.* [Online] 2008. [Cited: May 25, 2012.] http://mechanical-transmission.com/productsdetails.asp?ID=173.

8. **Taylor Race Engineering.** *Taylor Race Engineering.* [Online] 2012. [Cited: May 25, 2012.] http://taylor-race.com/.

9. **Fletcher, Herman S.** *Experimental Investigation of Lift, Drag, and Pitching Moment of Five Annular Airfoils.* Langley Field, Va : National Advisory Committee for Aeronautics, October, 1957. TN 4117.

10. **Ribner, Herbert S.** *The Ring Airfoil in Nonaxial Flow.* Langley, Virginia : National Advisory Committee for Aeronautics, 1947.

11. **Faulhaber.** Brushless DC-Servomotors, Series 1226...B. *Faulhaber.* [Online] 2012. [Cited: May 29, 2012.] http://www.faulhaber.com/uploadpk/EN_1226_B_MIN.pdf.

12. —. Planetary Gearheads Series 12/4. *Faulhaber.* [Online] 2012. [Cited: May 29, 2012.] http://www.faulhaber.com/uploadpk/EN_12-4_MIN.pdf.

13. **The Timken Company.** Super Precision Thin-Section Instrument Ball Bearings Catalog. Keene, New Hampshire : The Timken Company, 2002.

14. **Budynas, Richard G. and Nisbett, J. Keith.** *Shigley's Mechanical Engineering Design.* New Delhi : Tata McGraw-Hill, 2011. pp. 579-580. ISBN-13:978-0-07-107783-5.

15. **Heatherington, Dale A.** Lewis Gear Strength Calculator. *Botlanta.org.* [Online] 2005. [Cited: June 1, 2012.] http://www.botlanta.org/converters/dale-calc/gear.html.

16. **Budynas, Richard G. and Nisbett, J. Keith.** *Shigley's Mechanical Engineering Design.* New Delhi : Tata Mcgraw-Hill, 2012. pp. 123-124. ISBN-13: 978-0-07-107783-5.